

Finite Source Effects in Strong Lensing: Implications for the Substructure Mass Scale

Gregory Dobler¹ & Charles R. Keeton²

¹*Department of Physics and Astronomy, University of Pennsylvania, 209 S. 33rd Street, Philadelphia, PA 19104 USA*

²*Department of Physics and Astronomy, Rutgers University, 136 Frelinghuysen Road, Piscataway, NJ 08854 USA*

18 June 2018

ABSTRACT

Flux ratio ‘anomalies’ in quadruply-imaged gravitational lenses can be explained with galactic substructure of the sort predicted by Λ CDM, but the strength and uniqueness of that hypothesis needs to be further assessed. A good way to do that is to use the physical scale associated with the size of the source quasar, and its dependence on wavelength. We develop a toy model to study finite source effects in substructure lensing. Treating substructure as a Singular Isothermal Sphere allows us to compute the images of a finite source analytically, and then to explore how the image configurations and magnifications depend on source position and size. Although simplified, our model yields instructive general principles: image positions and magnifications are basically independent of source size until the source is large enough to intersect a substructure caustic; even sources that are much larger than the substructure Einstein radius can be perturbed at a detectable level; and most importantly, there is a tremendous amount to be learned from comparing image positions and magnifications at wavelengths that correspond to different source sizes.

In a separate analysis, we carefully study four observed radio lenses to determine which of the images are anomalous. In B0712+472, the evidence for a radio flux ratio anomaly is marginal, but if the anomaly is real then image C is probably the culprit. In B1422+231, the anomaly is in image A. Interestingly, B2045+265 and B1555+375 both appear to have *two* anomalous images. Coincidentally, in each system one of the anomalies is in image C, and the other is in either image A or image B (both possibilities lead to acceptable models). It remains to be seen whether Λ CDM predicts enough substructure to explain multiple anomalies in multiple lenses. When we finally join our modeling results and substructure theory, we obtain lower bounds on the masses of the substructures responsible for the observed anomalies. The mass bounds are broadly consistent with expectations for Λ CDM. Perhaps more importantly, we outline various systematic effects in the mass bounds; poor knowledge of whether the substructure lies within the main lens galaxy or elsewhere along the line of sight appears to be the dominant systematic.

Key words: cosmology: theory – dark matter – gravitational lensing

1 INTRODUCTION

While the Λ CDM cosmological scenario has been quite successful in describing measurements of cosmological structures on large scales (e.g., Tegmark et al. 2002; Dodelson et al. 2002; Spergel et al. 2003), it seems to overpredict the number of galactic satellites by about an order of magnitude (Klypin et al. 1999; Moore et al. 1999). The discrepancy could be resolved by modifying dark matter – making it warm, self-interacting, or otherwise exotic to reduce the predicted amount of small-scale structure (e.g., Colin et al. 2000; Spergel & Steinhardt 2000). Another possibility is that star formation in low-mass haloes is suppressed by photoionization (e.g., Bullock, Kravtsov, & Weinberg 2000; Somerville 2002; Benson et al. 2002), which would mean that many small haloes are present by dark. The latter hypothesis is readily tested with gravitational lensing, which is sensitive to the distribution of both luminous and dark matter over a range of scales in galaxy haloes.

Strong gravitational lensing has long been known to probe galaxy mass distributions on kiloparsec scales (e.g., Refsdal 1964; Young et al. 1981; Kochanek 1991), and even to be sensitive to the fine graininess of stellar mass distributions (microlensing; e.g., Chang & Refsdal 1979; Wambsganss 2001). More recently, Mao & Schneider (1998) pointed out that lensing is also sensitive to structure on intermediate scales ($\ell \sim \text{few pc}$, $M \sim 10^6 M_\odot$). This effect, sometimes termed ‘millilensing,’ could solve a long-standing problem in lens modeling. Detailed mass models of quadruply-imaged lenses are quite successful at matching the relative positions of the images, but often fail to reproduce the relative fluxes. Mao & Schneider pointed out that intermediate-scale substructure could nicely explain the ‘anomalous’ flux ratios in radio lenses, taking the troublesome lens B1422+231 as their example. Later, Metcalf & Madau (2001) connected this idea to the predictions of Λ CDM and suggested that the statistical distribution of lens flux ratios could be used to test the hypothesis that galaxies contain significant substructure. Dalal & Kochanek (2002) carried out the statistical test for seven quadruply-imaged quasars to infer that the fraction of galactic mass in substructure is $2.0_{-1.4}^{+5.0}$ per cent (90 per cent confidence), which seemed to match the amount of substructure expected for Λ CDM, and to rule out modified dark matter models.

Connecting observed flux ratio anomalies to inferences about dark matter requires a fairly long chain of logic, whose strength is still being assessed. The very first link is the identification of flux ratio anomalies. Careful analysis of the lens mapping reveals model-independent relations between certain images in 4-image lenses with ‘cusp’ or ‘fold’ configurations, relations which can only be violated if the lens galaxy contains significant small-scale structure (Keeton et al. 2003; Gaudi et al. 2005). As valuable as that analysis is, it only reveals which lens *systems* contain anomalies; it does not pinpoint which individual *images* are anomalous. This issue is crucial because lens theory predicts fundamental differences in how positive- and negative-parity images are affected by small-scale structure (Schechter & Wambsganss 2002; Keeton 2003), which offers a key test of the substructure hypothesis that may rule out competing explanations of flux ratio anomalies (see Kochanek & Dalal 2004). Furthermore, the large number of substructures implied by Λ CDM (e.g., Cooray & Sheth 2002; Sheth & Jain 2003) suggests the possibility that more than one image could be perturbed, but previous analyses have not determined whether that actually occurs. One goal of our analysis is to revisit models of flux ratio anomaly lenses to see if we can figure out which of the images are affected by substructure.

Another link in the chain of logic involves determining the length or mass scale associated with flux ratio anomalies. According to the substructure hypothesis, the anomalies are caused by mass clumps in the range $M \sim 10^6\text{--}10^8 M_\odot$, corresponding to a length scale of a few to tens of parsecs. However, violations of the cusp and fold relations really only indicate structure on the scale of the separation between images (see Keeton et al. 2003), which is typically no smaller than a few tenths of an arcsecond, or hundreds of parsecs. The difference in scale means that substructure cannot yet be established as the only viable explanation for flux ratio anomalies (e.g., Evans & Witt 2003; but see Kochanek & Dalal 2004). Moreover, even within the substructure hypothesis, comparisons between the predicted and inferred amount of substructure are very sensitive to scale.

The size of the source quasar brings an additional scale into the problem. Heuristically, a source ‘feels’ lensing structure only on scales larger than itself. Combining conventional wisdom about structure in lens galaxies with the standard model of quasars (e.g., Peterson 1997; Krolik 1999), it is believed that quasar optical continuum light is very sensitive to both microlensing and millilensing; that the optical broad emission lines are certainly sensitive to millilensing and may or may not be affected by microlensing (see Abajas et al. 2002; Lewis & Ibatá 2004; Richards et al. 2004); that the radio and mid-IR light can only be affected by millilensing; and that the optical narrow emission lines should not be affected by any small-scale structure. Measuring the flux ratios associated with several different source sizes could therefore provide a way to determine the substructure scale (Moustakas & Metcalf 2003). Dalal & Kochanek (2002) used these ideas in a general way, selecting radio lenses in order to focus on millilensing (and ignore microlensing). Wisotzki et al. (2003) compared the optical continuum and broad line flux ratios for HE 0435–1223 to infer that there must be microlensing in that system, and maybe some millilensing as well. Metcalf et al. (2004) compared the optical narrow line flux ratios with the radio and mid-IR flux ratios for Q2237+0305 to find evidence for millilensing and place limits on the substructure mass scale.

Despite this evidence for the value of working with different source sizes, there has been no general study of source size effects in millilensing. The second main goal of our paper is to present a semi-analytic toy model that allows us to examine a wide range of finite source effects. Assuming that any given flux ratio anomaly is caused by a single, isolated clump that can be modeled as an isothermal sphere is admittedly a toy model – but in the best sense of the term: a tool that not only reveals, but also elucidates, some interesting general principles. As we completed our work, we learned that Inoue & Chiba (2004) recently considered the same toy model and derived analytic approximations for the millilensing magnification in the limit of a large source. Our work complements theirs by presenting exact results for a large range of source sizes, by considering some of the effects in more details, and also by applying the general theory to four specific observed lenses.

Thus our paper has two main goals: to better understand the flux ratio anomalies in four observed radio lenses; and to study finite source effects in millilensing. The two parts are independent of each other, although we do combine them in the end to place constraints on the substructures required to produce the observed flux ratio anomalies. Pedagogically, it makes sense to begin with the study of finite source effects. In §2 we develop our toy model for millilensing and use it to study the image configurations and magnifications for different source sizes and positions; the discussion goes into some depth, so we

offer a review of the main points in §2.6. In §3 we introduce a method for using our millilensing theory can to place lower bounds on the masses of substructures responsible for flux ratio anomalies. In §4 we turn to the analysis of real lens systems; we first use lens models to determine which images are anomalous, and then apply our millilensing theory to derive the substructure mass bounds. We summarize our results and conclusions in §5. Throughout the paper we assume a cosmology with $\Omega_M = 0.3$, $\Omega_\Lambda = 0.7$, and $h = 0.7$.

2 SIS IMAGES OF A FINITE SOURCE

This section presents our toy model for studying the effects of a finite source size. We define the model and then consider the image configurations and magnifications as a function of the position and size of the source. Although the focus is millilensing, our results have some broader implications that are discussed in §2.6.

2.1 Macromodel

In lens modeling, it is common to begin with a smooth ‘macromodel’ that reproduces the number and positions of the lensed images. Smooth models generally fail to fit the observed flux ratios, so small clumps are introduced that modify the flux ratios enough to fit the data. (The clumps may modify the image positions as well, but not by much more than current measurement errors; see §2.5.) To understand the effects of a clump near one of the lensed images, we zoom in and consider the lens mapping only in the vicinity of the clump. The clump is small compared with the galaxy ($R_{\text{clump}}/R_{\text{gal}} \sim 10^{-3}$), so on this scale the macromodel can be approximated as a constant convergence and shear (κ and γ , respectively). The image magnification predicted by the macromodel is

$$\mu_0 = |(1 - \Gamma)^{-1}| = \frac{1}{(1 - \kappa)^2 - \gamma^2}, \quad (1)$$

where $1 - \Gamma$ is the local lens mapping (in coordinates aligned with the local shear for simplicity),

$$1 - \Gamma = \begin{bmatrix} 1 - \kappa - \gamma & 0 \\ 0 & 1 - \kappa + \gamma \end{bmatrix}. \quad (2)$$

We can distinguish between three types of images based on the eigenvalues of this matrix. Positive parity images have $1 - \kappa + \gamma > 1 - \kappa - \gamma > 0$. Negative parity images have $1 - \kappa + \gamma > 0 > 1 - \kappa - \gamma$, so they are parity reversed in one direction. Double negative parity images have $1 - \kappa - \gamma < 1 - \kappa + \gamma < 0$, so they are parity reversed in both directions; however, images of this type are faint, rarely observed, and of relatively little importance for substructure lensing (e.g., Winn, Rusin, & Kochanek 2004). For the special case of an isothermal ellipsoid macromodel, $\kappa = \gamma$ everywhere.

Many studies of millilensing have assumed that the clump lies in the halo of the main lens galaxy, but Keeton (2003) and Metcalf (2004) have pointed out that a clump elsewhere along the line of sight could still have a significant effect. While one can invoke statistical arguments about whether a clump is more likely to lie in the galaxy or along the line of sight (e.g., Chen et al. 2003), strictly speaking the clump redshift is unknown and that may lead to a systematic uncertainty in a millilensing analysis. Fortunately, this effect is easily accommodated in our formalism. Keeton (2003) showed that if the clump does lie at a different redshift than the lens galaxy, the macromodel can still be treated as a simple convergence and shear, but with effective values

$$\begin{aligned} \kappa_{\text{eff}} &= \frac{(1 - \beta)[\kappa - \beta(\kappa^2 - \gamma^2)]}{(1 - \beta\kappa)^2 - (\beta\gamma)^2}, \\ \gamma_{\text{eff}} &= \frac{(1 - \beta)\gamma}{(1 - \beta\kappa)^2 - (\beta\gamma)^2}, \end{aligned} \quad (3)$$

where $\beta = (D_{cl}D_{os})/(D_{ol}D_{cs})$ for a foreground clump ($z_c < z_l$), while $\beta = (D_{lc}D_{os})/(D_{oc}D_{ls})$ for a background clump ($z_l < z_c < z_s$). In what follows we simply use κ and γ to denote the macromodel, bearing in mind that we should use the effective values if we want to consider a line-of-sight clump.

Another possible systematic effect arises from the ‘mass sheet degeneracy’ in the macromodel. Adding a uniform mass sheet (and rescaling the galaxy mass appropriately) leaves the image positions and flux ratios unchanged (Gorenstein et al. 1988; Saha 2000). Turning the problem around, lens models cannot detect the presence of a mass sheet, which can bias the conclusions drawn from the models (Keeton & Zabludoff 2004). We should therefore consider how a mass sheet might affect a millilensing analysis. For our purposes, adding a mass sheet of density κ_{sheet} is equivalent to a simple rescaling of the macromodel:

$$\begin{aligned} \kappa' &= (1 - \kappa_{\text{sheet}})\kappa + \kappa_{\text{sheet}}, \\ \gamma' &= (1 - \kappa_{\text{sheet}})\gamma. \end{aligned} \quad (4)$$

This rescaling is the same no matter whether the clump lies in the lens galaxy or along the line of sight.

2.2 Micromodel

We model the mass clump as a singular isothermal sphere (SIS). One of the advantages of the SIS is that its $\rho \propto r^{-2}$ density profile yields a simple form for the deflection angle,

$$\alpha(\mathbf{x}) = b \frac{\mathbf{x}}{|\mathbf{x}|}, \quad (5)$$

where the Einstein radius b is

$$b = 4\pi \left(\frac{\sigma}{c}\right)^2 \frac{D_{ls}}{D_{os}}. \quad (6)$$

Here, σ is the velocity dispersion of the SIS, while D_{os} and D_{ls} are angular diameter distances from the observer or lens to the source. Although N-body simulations predict a different form for the density profile of dark matter structures (e.g., Navarro, Frenk, & White 1996), the SIS has been used for modeling substructures in previous studies (Metcalf & Madau 2001; Dalal & Kochanek 2002), and its simplicity makes it an attractive choice for a toy model whose purpose is to yield general insights. The mass of the SIS increases linearly with radius, and the projected 2-D mass within the Einstein radius is

$$M(b) = \frac{c^2}{4G} \frac{D_{os}}{D_{ol}D_{ls}} b^2 = \pi \Sigma_{\text{cr}} b^2, \quad (7)$$

where $\Sigma_{\text{cr}} = c^2 D_{os} / (4\pi G D_{ol} D_{ls})$ is the critical surface density for lensing.

The clump + macromodel system is governed by the lens equation

$$\begin{aligned} u &= (1 - \kappa - \gamma)r \cos \theta - b \cos \theta, \\ v &= (1 - \kappa + \gamma)r \sin \theta - b \sin \theta, \end{aligned} \quad (8)$$

where $\mathbf{u} = (u, v)$ are coordinates in the source plane and $\mathbf{x} = (r \cos \theta, r \sin \theta)$ are coordinates in the image plane (centred on the clump). In substructure lensing, solutions of this lens equation represent ‘micro-images’ that are not separately resolved but combine to form the observed macro-image. For a point source, the individual micro-image magnifications are given by

$$\mu^{-1} = \left| \frac{\partial \mathbf{u}}{\partial \mathbf{x}} \right| = \mu_0^{-1} - \frac{b}{r} (1 - \kappa - \gamma \cos 2\theta). \quad (9)$$

The tangential critical curve for the lens system can be found by taking $\mu \rightarrow \infty$, which yields

$$r_{\text{crit}}(\theta) = \frac{b(1 - \kappa - \gamma \cos 2\theta)}{(1 - \kappa)^2 - \gamma^2}. \quad (10)$$

Plugging this into the lens equation then gives a parametric equation for the tangential caustic. The radial pseudo-caustic is the curve in the source plane that maps to the origin in the image plane; from eq. (8), it can be written parametrically as

$$u_p = -b \cos \theta, \quad (11)$$

$$v_p = -b \sin \theta. \quad (12)$$

It can be seen from equations (8) and (9) that the positions and magnifications of the images of a point source depend on the perturber strength b , the position of the source relative to the perturber, and κ and γ from the macromodel. There is no general analytic solution to the lens equation even for a simple SIS perturber. Nevertheless, it is possible to find an analytic solution for a source of *finite* size at an arbitrary position. Finch et al. (2002) showed how to compute the area enclosed by the caustics of an SIS lens in an external shear field, and in the following sections we extend their method to find the positions, shapes, and magnifications of the images of a finite source lensed by an SIS in a convergence and shear field.

2.3 Analytic solution for the images of a finite source

First, we consider a circular source and parametrize its boundary:

$$u = u_0 + a \cos(\lambda), \quad (13)$$

$$v = v_0 + a \sin(\lambda), \quad (14)$$

where u_0 and v_0 are the coordinates of the centre of the source, a is the source size, and λ varies from 0 to 2π . (Finch et al. considered the special case $u_0 = v_0 = 0$ and $a = b$.) Plugging the source boundary into the lens equation (8) yields

$$a \cos(\lambda) = (1 - \kappa - \gamma)r \cos \theta - b \cos \theta - u_0, \quad (15)$$

$$a \sin(\lambda) = (1 - \kappa + \gamma)r \sin \theta - b \sin \theta - v_0. \quad (16)$$

We can eliminate λ by squaring and adding these two equations to obtain

$$0 = r^2 \Gamma_-^2 \cos^2 \theta + r^2 \Gamma_+^2 \sin^2 \theta - 2u_0 \Gamma_- r \cos \theta - 2v_0 \Gamma_+ r \sin \theta - 2\Gamma_- r b \cos^2 \theta - 2\Gamma_+ r b \sin^2 \theta + u_0^2 + v_0^2 + b^2 - a^2 + 2u_0 b \cos \theta + 2v_0 b \sin \theta, \quad (17)$$

where $\Gamma_{\pm} = (1 - \kappa \pm \gamma)$. This is a quadratic equation for $r(\theta)$ whose solution yields the boundary of the image(s):

$$r_{\pm}(\theta) = \frac{A \pm \sqrt{B}}{C}, \quad (18)$$

where

$$\begin{aligned} A &= -2u_0(\gamma + \kappa - 1) \cos \theta - 2b(\gamma \cos 2\theta + \kappa - 1) + 2v_0(\gamma - \kappa + 1) \sin \theta, \\ B &= -4[\gamma^2 + (\kappa - 1)^2 + 2\gamma(\kappa - 1) \cos 2\theta] [b^2 - a^2 + u_0^2 + v_0^2 + 2b u_0 \cos \theta + 2b v_0 \sin \theta] \\ &\quad + 4[u_0(\kappa + \gamma - 1) \cos \theta + b(\kappa + \gamma \cos 2\theta - 1) + v_0(\kappa - \gamma - 1) \sin \theta]^2, \\ C &= 2[\gamma^2 + (\kappa - 1)^2 + 2\gamma(\kappa - 1) \cos 2\theta]. \end{aligned}$$

Though complicated, this is a completely analytic mapping of the boundary of the source to the boundary of the image(s).

While eq. (18) completely describes the image boundary, it is important to note that only solutions with $r_{\pm}(\theta)$ real and positive are physical. For some parameter combinations, B can be negative which implies that \sqrt{B} , and hence $r_{\pm}(\theta)$, is complex. In particular, for given values of $(\gamma, \kappa, a, b, u_0, v_0)$, B may or may not be negative for a particular θ . The range of θ for which $B \geq 0$ defines the azimuthal extent of the image(s). In addition, there are also parameter combinations for which $r_{\pm}(\theta) < 0$. Such solutions are not physical and form the boundaries of an ‘artefact’ image.

The $r_{\pm}(\theta)$ solutions shown in Fig. 1 exhibit both of these features. For this example, $\kappa = \gamma = 0.3$ so the unperturbed image has positive parity and magnification $\mu_0 = 2.5$. Panels (a) and (b) show $r_{\pm}(\theta)$ which are real for only certain values of θ . Physically this implies that the images have a finite azimuthal extent, as can be seen in panel (c). Panel (b) also shows that there is a range of θ where $r_{-}(\theta) < 0$. This corresponds to the unphysical artefact image shown by the dotted line in panel (c).

Fig. 2 shows how image configurations change as the source size a is increased. The left column shows the source and the caustics while the right column shows the images and the critical curves; without loss of generality, we work in units with $b = 1$. For the top row, the source with $a = 0.01$ has been placed near a fold caustic but has not intersected it. The source lies completely within a two-image region and the $r(\theta)$ solution does in fact give two images. In the second row, the source has doubled in size and now crosses the fold caustic. In this configuration, part of the source lies in the two-image region and another part lies in the four-image region. The $r(\theta)$ solution shows that the initial two images have grown slightly in size and a third image (which is actually a merged image pair) has appeared in the upper left. As the source size is increased further, it crosses more and more of the caustics yielding complex image solutions which consist of merging and growing images. By $a = 1.2$, the source covers most of the caustic and the resulting image is clearly becoming the ellipse that one would expect for a simple convergence and shear field. Nevertheless, even at this large source size there are still significant deviations from the unperturbed image.

Fig. 3 is similar to Fig. 2 except that the unperturbed image has negative parity with $\kappa = \gamma = 0.7$ ($\mu_0 = -2.5$), and we use a different source position. Between $a = 0.04$ and $a = 0.15$, the source crosses the caustic separating the two and three-image regions, and the image configurations show the appearance of a small third image near the origin. By $a = 0.2$, the source has intersected the caustic again, which corresponds to the merging of two of the images. Increasing the source further results in the growth and merger of the images, and by $a = 1.2$ we are again beginning to see the ellipse that would be expected from only the convergence and shear field.

2.4 Magnification of a finite source

Having found the image configurations for finite sources, we now seek the magnifications. Since gravitational lensing conserves surface brightness, the change of flux is due solely to the change in size of the source when it is lensed. If the source has a uniform surface brightness, then the magnification is the ratio of the area of the image(s) to the area of the source.

Our parametric solution for the image boundaries allows us to compute the image area, if we take care to understand the different solution regimes. Where $r_{+}(\theta)$ and $r_{-}(\theta)$ are real and positive, they form the outer and inner boundaries (respectively) of the images (see Fig. 4). The image area is then

$$\frac{1}{2} \int_I [r_{+}^2(\theta) - r_{-}^2(\theta)] d\theta, \quad (19)$$

where I is the range of θ over which the solution is defined (i.e., where $B \geq 0$). If only $r_{+}(\theta)$ is real and positive, it forms the complete boundary of the image and the image area is $\frac{1}{2} \int_I r_{+}^2(\theta) d\theta$. Finally, where $r_{+}(\theta)$ and $r_{-}(\theta)$ are both negative,

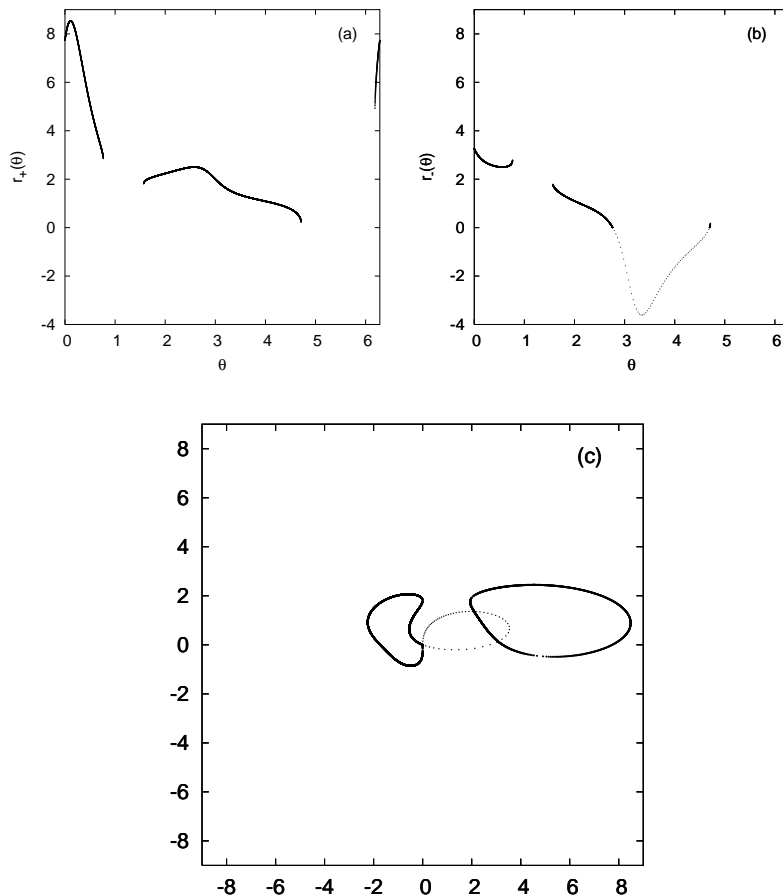


Figure 1. Analytic image boundary solutions for $\kappa = \gamma = 0.3$, $(u_0, v_0) = (1.2, 0.8)$, and $(a, b) = (1.2, 1.0)$. (a) $r_+(\theta)$ versus θ . The region of θ where $r_+(\theta)$ is defined gives the azimuthal extent of the images. (b) $r_-(\theta)$ versus θ . The dotted line indicates where $r_-(\theta)$ is real but negative, which corresponds to an unphysical ‘artefact’ image. (c) Image boundaries in the (x, y) plane. Solid lines show the physical solutions, while the dotted line shows the artefact image with $r_-(\theta) < 0$.

there is no contribution to the image area. (Note that $r_- < r_+$ for all parameter values and all θ , so there is never an area contribution due to $r_-(\theta)$ alone.)

Thus, the total magnification (ratio of image size to source size) can be written as,

$$\mathcal{M} \equiv \frac{\mu}{\mu_0} = \frac{1}{2\pi\mu_0 a^2} \int d\theta \begin{cases} r_+^2(\theta) - r_-^2(\theta) & \text{if } B > 0 \text{ and } A > \sqrt{B} \\ r_+^2(\theta) & \text{if } B > 0 \text{ and } A < \sqrt{B} \\ 0 & \text{if } B < 0 \text{ or } A + \sqrt{B} < 0 \end{cases} \quad (20)$$

Since we are primarily interested in how much the flux *changes* due to the presence of the SIS perturber, we have normalized eq. (20) with respect to the magnification μ_0 produced by the convergence and shear alone. We refer to this as the ‘normalized magnification.’ Unfortunately, the integral in eq. (20) cannot be evaluated analytically. Still, it requires only a one-dimensional numerical integral, which means that the analytic solution of the lens equation yields a much faster calculation than a conventional two-dimensional numerical integral. Inoue & Chiba (2004) give analytic approximations for \mathcal{M} in the limit of a large source (also see Appendix A), but we are interested in the exact result for a wide range of source sizes.

We can now understand the effects that the mass sheet degeneracy in the macromodel have on the substructure analysis. Adding a mass sheet rescales the macromodel as shown in eq. (4). From eqs. (1) and (18), we then see that μ_0 and r_{\pm}^2 are both rescaled as $(1 - \kappa_{\text{sheet}})^{-2}$. As a result, the normalized magnification \mathcal{M} is *unchanged* by the addition of the mass sheet. We conjecture that this result is special to the SIS clump model, and it would be interesting to consider other clump models. However, for our purposes the remarkable implication is that our substructure analysis is completely unaffected by the mass sheet degeneracy.

Fig. 5 shows the normalized magnification as a function of source size for the source from Fig. 2. The curve has several notable features that can be understood in terms of the image configurations in Fig. 2. First, for $a \lesssim 0.01$ the source does

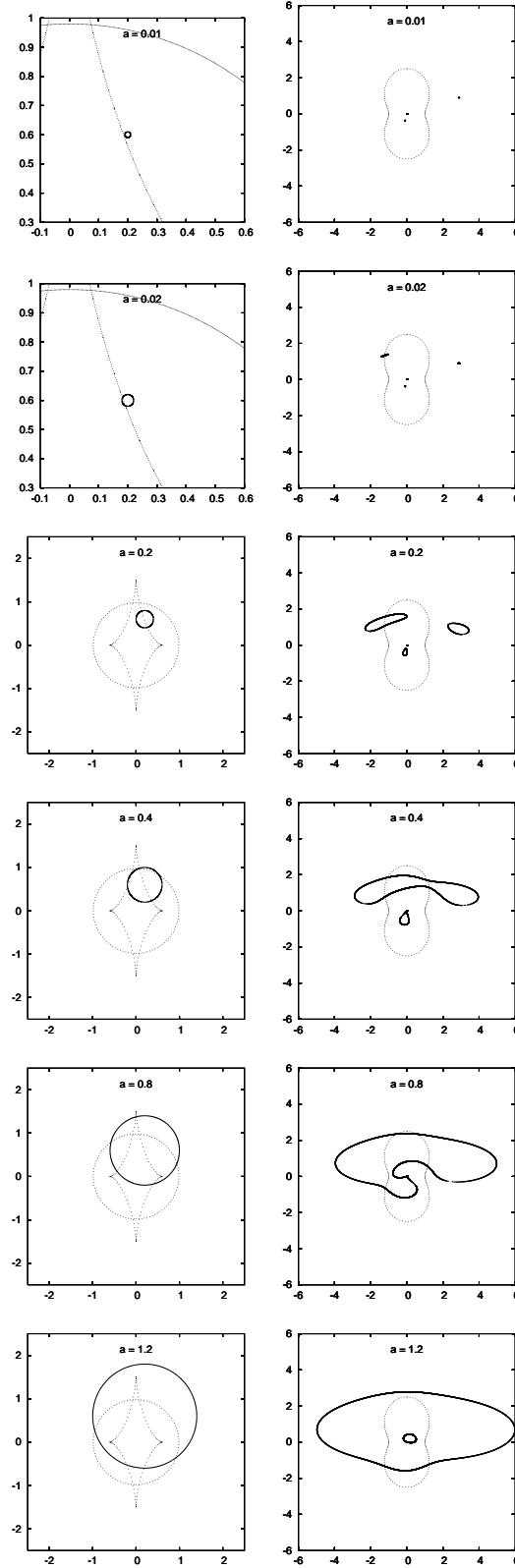


Figure 2. Image configurations for different source sizes. The left column shows the source boundaries and caustics, while the right column shows the image boundaries and critical curves. In these examples, $\kappa = \gamma = 0.3$, $(u_0, v_0) = (0.2, 0.6)$, $b = 1$, and a is increased from 0.01 to 1.2. At large source size ($a/b > 1$) there are still significant deviations from the ellipse image expected for a pure convergence and shear field.

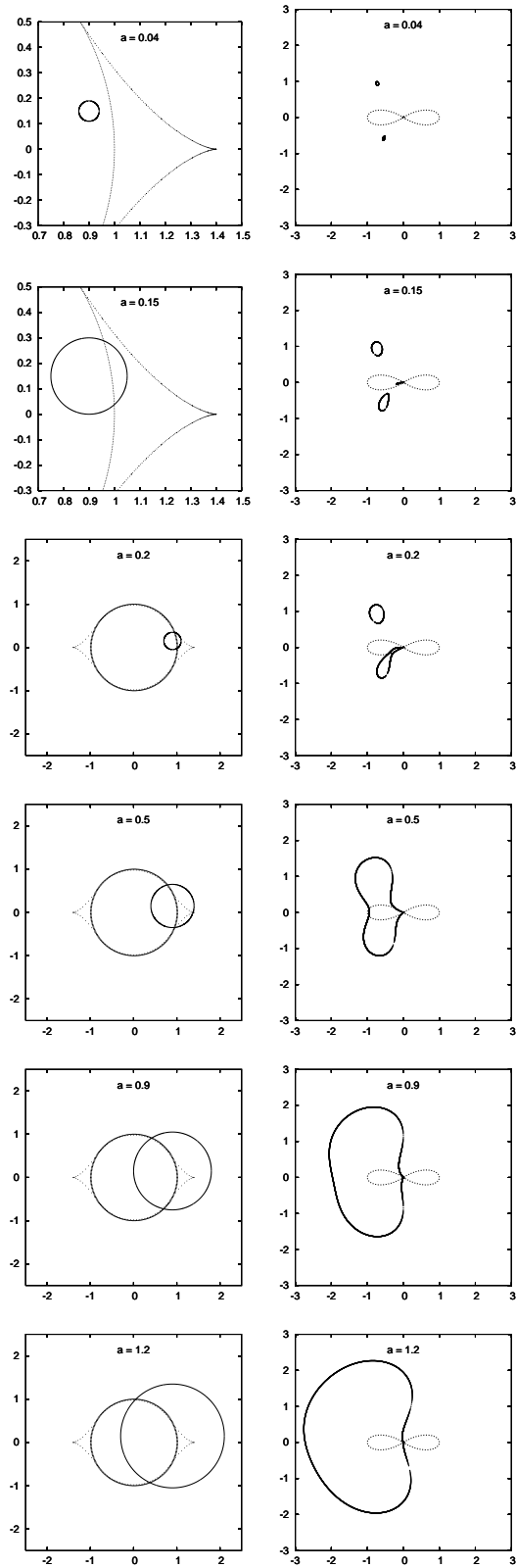


Figure 3. Similar to Fig. 2, but for negative parity. In these examples, $\kappa = \gamma = 0.7$, $(u_0, v_0) = (0.9, 0.15)$, $b = 1$, and a is increased from 0.04 to 1.2.

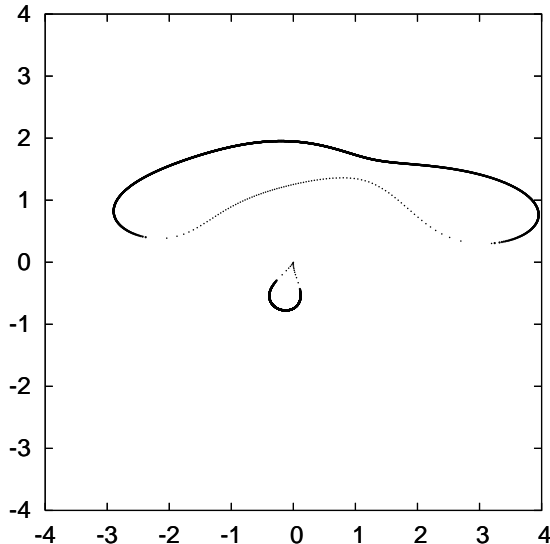


Figure 4. Image configuration for $\kappa = \gamma = 0.3$, $(u_0, v_0) = (0.2, 0.6)$, $(a, b) = (0.1, 1.0)$. The solid line shows $r_+(\theta)$, which forms the outer boundary of the images. The dotted line shows $r_-(\theta)$, which forms the inner boundary.

not come into contact with the caustics and the magnification is basically independent of source size. The sharp increase in magnification between $a = 0.01$ to 0.02 corresponds to the appearance of a third image as the source begins to cross the fold caustic. The magnification then comes to a large peak, followed by a smaller peak near $a = 0.8$. Comparing to the fourth row of Fig. 2, we see that this secondary peak occurs when the source begins to come into contact with the caustic cusps. Finally, as a becomes large, the magnification approaches unity; that is, for large sources the effect of the SIS perturber becomes negligible, as expected. Nevertheless, it should be noted that even at $a/b = 50$, the image flux is still perturbed by 3.7 per cent.

Fig. 6 shows the normalized magnification as a function of a for the source from Fig. 3. The parameters here are the same as the previous figure except that this case has negative parity ($\kappa = \gamma = 0.7$). For an SIS clump in front of a negative parity image, most source positions yield *demagnification* relative to the background convergence and shear field (Keeton 2003). Indeed, for this position the normalized magnification is less than 1 for most source sizes. However, there is a region of magnification (relative to the convergence and shear field) for $0.1 \lesssim a \lesssim 1.0$. We can again match some of the features of this plot to the image configurations from Fig. 3. There is very little change in the normalized magnification until $a \approx 0.1$, which corresponds to the source coming into contact with the caustic. There is a peak at $a \approx 0.2$ as the source starts to come into contact with the caustic cusp, followed by a shallow dip at $a \approx 0.3$ as the source begins to occupy more of the demagnification region of the source plane. As the source size is increased further, there is then another maximum followed by a minimum at $a \approx 2$. The normalized magnification for this negative parity case also approaches unity for large a , with the flux at $a/b = 50$ differing from unity by 1 per cent. Comparing the positive and negative parity cases gives the interesting result that, at large a , an SIS perturber has less effect on the magnification of a negative parity image than on an equivalent positive parity image.

Since the magnification is largely determined by encounters with caustics, we now study how the magnification versus source size curve changes as the source *position* is varied. Fig. 7 shows the normalized magnification curves for different source positions, for a positive parity case ($\kappa = \gamma = 0.3$). The upper left panel shows the caustics and source positions for the plot's other panels, and the upper right panel shows the normalized magnification curve for the source located at the origin.

Most of these curves have at least one, and in some cases two, peaks where the normalized magnification increases sharply. These peaks are, in general, associated with the source boundary crossing a caustic. It should also be noted that, while some peak heights are relatively low with a normalized magnification of around 2, the normalized magnification can become as high as about 16 (second row middle column). This case is particularly illuminating as the main peak turns out to coincide with the source crossing the upper cusp caustic while the secondary peak around $a \sim 1.0$ corresponds to the source coming into contact with the left and right cusps. The next panel (row three column two) is also notable for the plateau at low values of a , and again there is a small secondary peak around $a \sim 1-2$ that corresponds to the source coming into contact with the left and right cusps. Finally, two general features of the plots are striking. First, all of the curves remain fairly constant at small a where the source does not intersect the caustics of the SIS, implying that the source does not ‘feel’ the structure of the perturber before it comes into contact with these caustics. Second, although all of the plots tend towards unity as expected

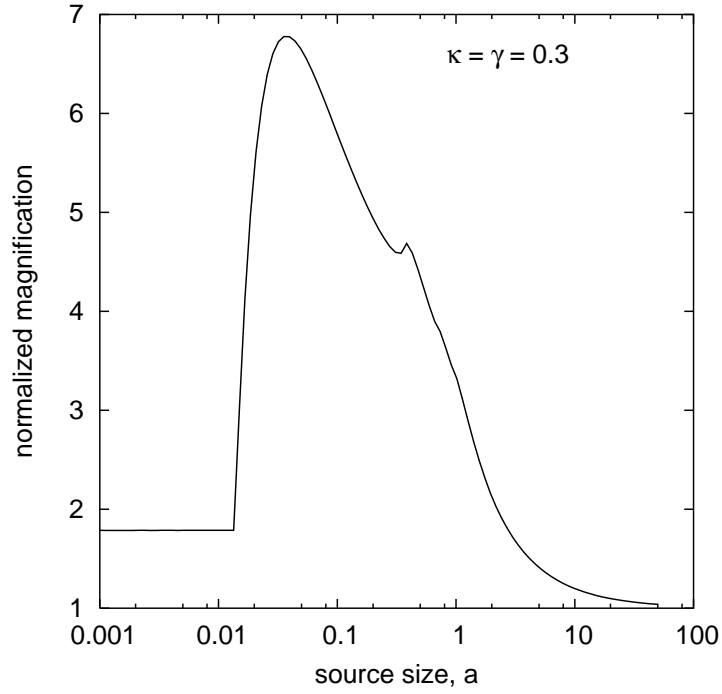


Figure 5. Normalized magnification as a function of source size for $\kappa = \gamma = 0.3$, $(u_0, v_0) = (0.2, 0.6)$, $b = 1$. The sharp increase at $a \approx 0.015$ corresponds to a transition from two images to three (see text).

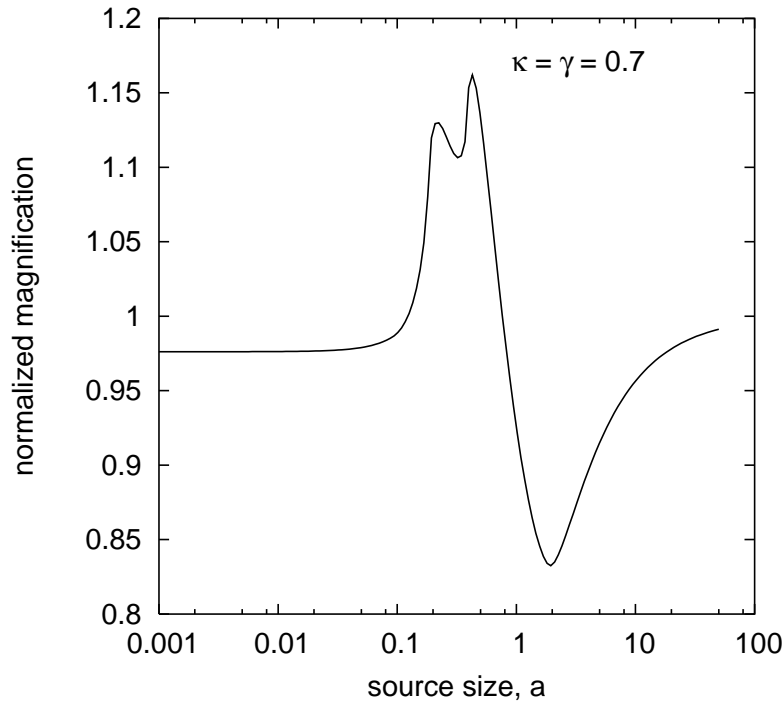


Figure 6. Similar to Fig. 5, but for $\kappa = \gamma = 0.7$, $(u_0, v_0) = (0.9, 0.15)$, $b = 1$. The features of the curve are due to the source coming into contact with the caustics, as shown in Fig. 3.

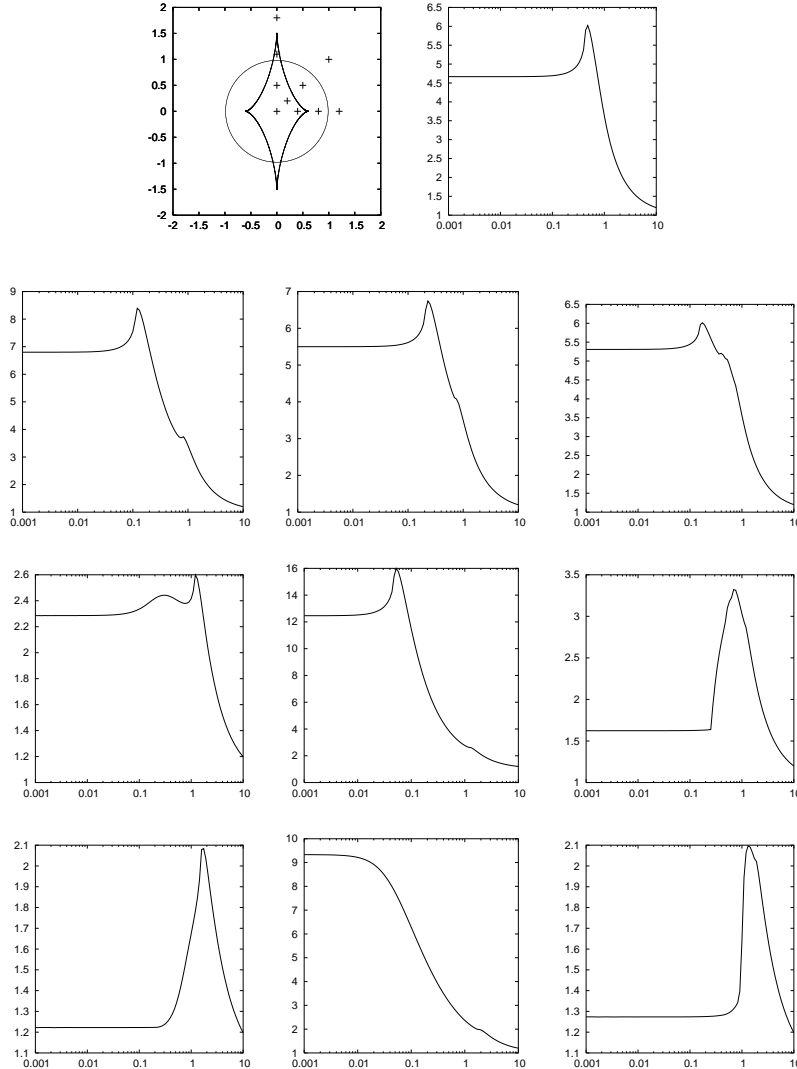


Figure 7. Normalized magnification as a function of source size for a positive parity case ($\kappa = \gamma = 0.3$), with $b = 1$. The top left panel shows the caustics and source positions. The top right panel shows the magnification curve for a source at the origin. The left column represents moving the source along u-axis, $u_0 = 0.4, 0.8, 1.2$ (top to bottom); the middle column represents moving along the v-axis, $v_0 = 0.5, 1.1, 1.8$; and the right column represents moving along the line $v_0 = u_0$, with $u_0 = 0.2, 0.5, 1.0$.

for a large source, they do seem to deviate from unity fairly uniformly at $a \gtrsim 10$; in particular, all of the magnifications are $\mathcal{M} \simeq 1.2$ at $a = 10$. In Appendix A we formalize this result by showing that the normalized magnification is independent of source position, to first order in $1/a$. Since it is possible to measure flux ratios with percent-level precision (after correcting for time delays; see Fassnacht et al. 2002), an important implication is that even large sources relatively far from the mass clump can be perturbed at a detectable level.

Fig. 8 shows the normalized magnification curves at various source positions for a negative parity case ($\kappa = \gamma = 0.7$). The behavior for the negative parity case is a bit more complex in that both magnification and demagnification (relative to the convergence and shear field) are seen. For example, at a source position of $u_0, v_0 = 1.1, 0.0$ (second row first column), the source is magnified at low a , rises to a peak at $a \simeq 0.2$, falls to a demagnified valley at $a \simeq 2$, and then rises toward unity for larger a . As in the positive parity case, we see that for small a there is relatively little structure in the curves. Also, the magnifications are again fairly uniform for $a \gtrsim 10$ (see Appendix A), with $\mathcal{M} \simeq 0.95$ at $a = 10$.

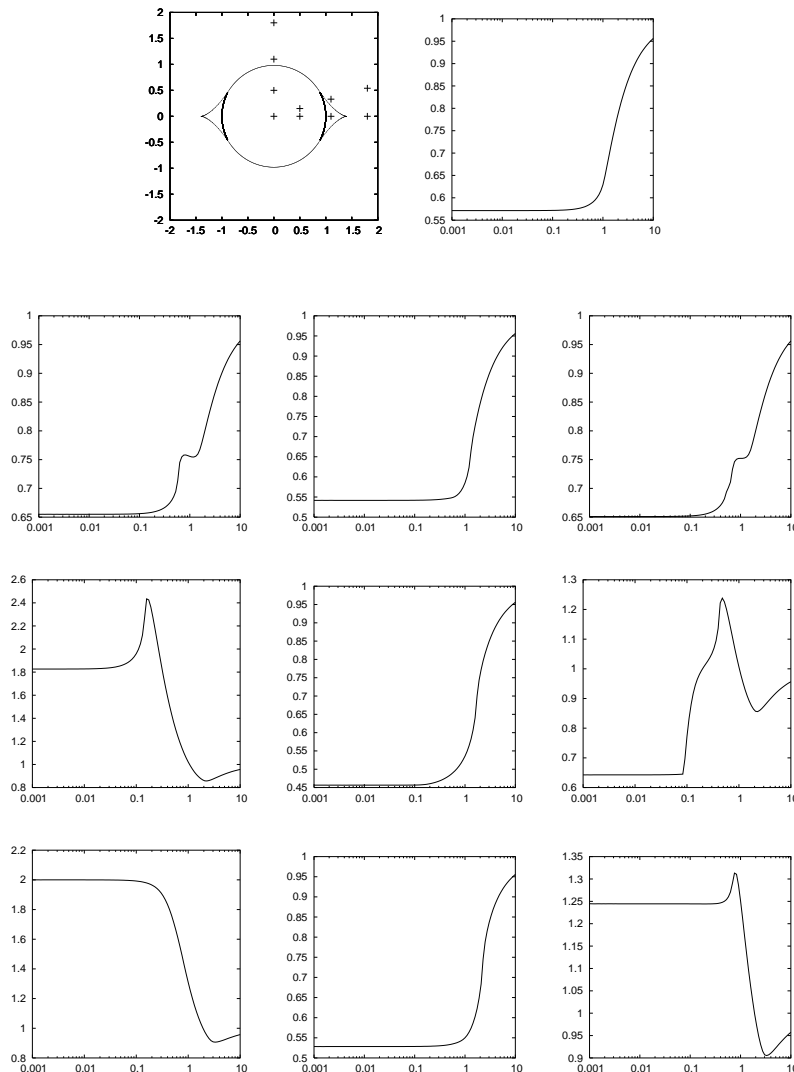


Figure 8. Similar to Fig. 7, but for a negative parity case ($\kappa = \gamma = 0.7$).

2.5 Center of flux position

Although we have determined the image boundary and magnification of a finite source, we have not yet quantified the image position. If the separate component images are not resolved, what matters is the ‘centre of flux’ of the image configuration, which can be computed as

$$\mathbf{X} = \frac{\int \mathbf{x} f(\mathbf{x}) d\mathbf{x}}{\int f(\mathbf{x}) d\mathbf{x}}, \quad (21)$$

where $f(\mathbf{x})$ is 1 inside the image and 0 outside. (This is the optical analog of the centre of mass.) The difference between this ‘centre of flux’ and the original image position in the absence of the clump, \mathbf{X}_0 , is the astrometric shift due to the perturber,

$$\delta\mathbf{X} = \mathbf{X} - \mathbf{X}_0. \quad (22)$$

Our solution for $r_{\pm}(\theta)$ yields a straightforward calculation for the astrometric perturbation, provided that we account for the different solution regimes as in eq. (20).

Fig. 9 shows the astrometric perturbation as a function of source size for the source from Fig. 2. As with the magnification calculation, we see that for a source size below about $a = 0.015$ the astrometric perturbation remains fairly constant. Comparison with the image configuration from Fig. 2 shows that the centre of flux position lies on the line joining the two images that are seen at $a = 0.01$. Between $a = 0.01$ and $a = 0.02$ there is a sudden change as the source intersects the caustic. The emergence of a bright third image rapidly pulls the centre of flux away from the line joining the initial two images.

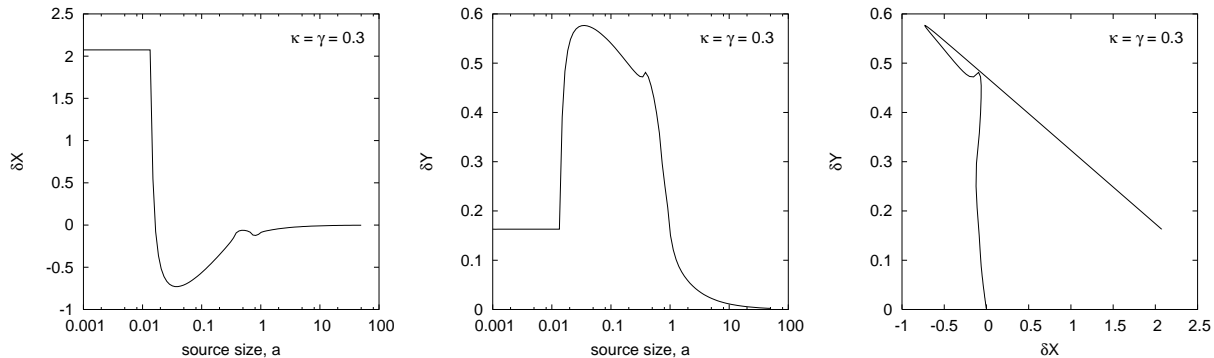


Figure 9. Astrometric perturbation as a function of source size for $b = 1$, $(u_0, v_0) = (0.2, 0.6)$, and $\kappa = \gamma = 0.3$. The large change between $a = 0.01$ – 0.02 corresponds a change from two to three images (see Fig. 2). For a large source, the perturber has little effect on the centre of flux position as expected.

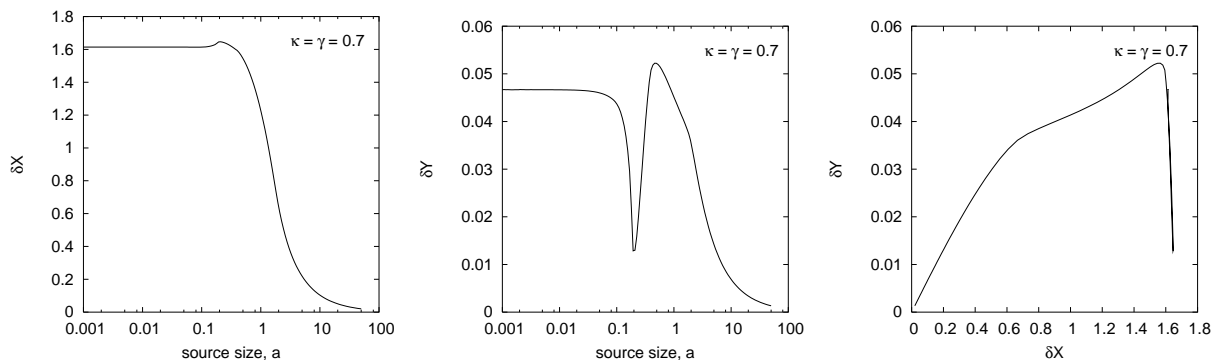


Figure 10. Astrometric perturbation as a function of source size for $b = 1$, $(u_0, v_0) = (0.9, 0.15)$, and $\kappa = \gamma = 0.7$. The large change at around $a = 0.2$ corresponds to the source intersecting a cusp caustic (see Fig. 3).

For a large source size, we would expect that the perturbing SIS would have little effect on the centre of flux of the image configuration and indeed as a gets large, the astrometric perturbation tends towards zero.

Fig. 10 shows the analogous results for a negative parity case with $\kappa = \gamma = 0.7$. There is not much change in the astrometric perturbation when a is less than about 0.1, but there is then a dramatic dip in both curves between $a = 0.01$ and 0.02. Returning to Fig. 3, we see that this large change in the centre of flux position occurs when the source begins to intersect the caustic.

Like stellar microlensing (e.g., Treyer & Wambsganss 2004), substructure lensing can produce astrometric shifts of order several Einstein radii. The difference is in the scale: the Einstein radius for stars is of order micro-arcseconds, while for substructure it is milli-arcseconds. Thus, astrometric perturbations due to substructure should be detectable with radio interferometry, and perhaps even with space-based optical or infrared imaging. While small position shifts might be degenerate with small changes in the macromodel, the dependence of the shift on source size (and hence wavelength) would provide a clear signature of substructure lensing. Astrometric shifts are related to shape perturbations (see Metcalf 2002), but do not require resolved image shapes. A full analysis of prospects for observing astrometric perturbations and using them to constrain substructure is beyond the scope of this paper, but warrants further study.

2.6 Comments

To review, we have studied how the magnification depends on the size of the source and its position relative to the caustics. The specific details depend on our assumption of an SIS clump, which is a toy model, but the basic principles should be more general. One point is that the image properties are basically independent of the source size until the source is large enough to encounter the caustics; that threshold of course depends on the source position. In the other extreme, sources more than an order of magnitude larger than the clump Einstein radius can still be perturbed at the percent level, and that precision

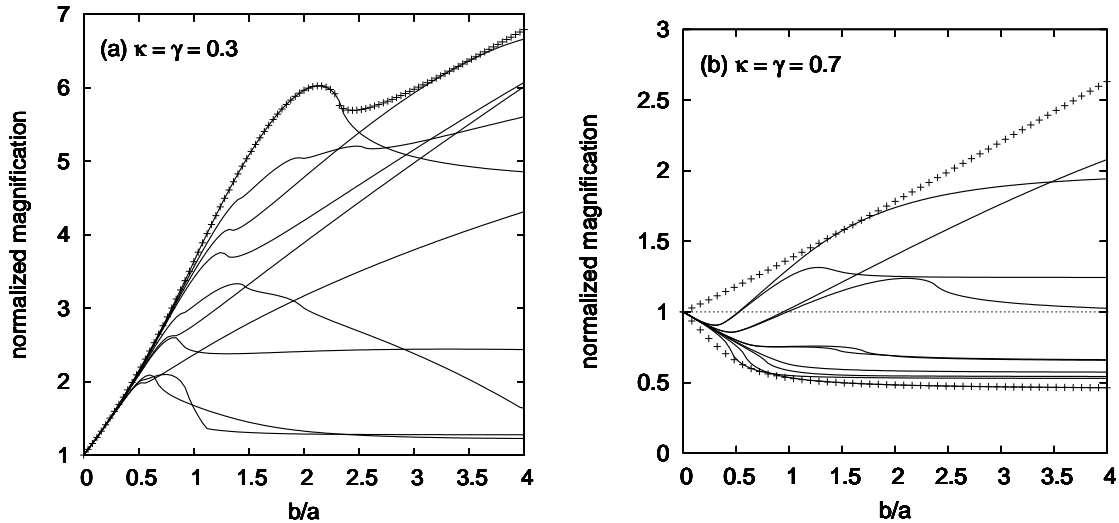


Figure 11. Normalized magnification as a function of b/a for a positive parity image (a) and a negative parity image (b). The crosses represent the maximum (maximized over source position) or minimum magnification for a given b/a . The solid lines show \mathcal{M} versus b/a at various fixed source positions, from Figs. 7 and 8.

can be obtained with careful observations (e.g., Fassnacht et al. 2002). In other words, the conventional wisdom that a source does not ‘feel’ lensing structure on scales smaller than itself is not really accurate beyond order of magnitude estimates.

In between these extremes, there is significant structure in the magnification versus source size curves. Therefore, in principle, comparing the flux of an image at different wavelengths corresponding to different source sizes could reveal a wealth of information about the size and location of substructure. Prospects for doing that are good: recent observations have demonstrated the ability to measure flux ratios not only for radio and optical continua, but also for optical emission lines and mid-IR emission (Agol et al. 2000; Wisotzki et al. 2003; Metcalf et al. 2004). We would advocate concerted effort to obtain and analyse such panchromatic observations of lenses with flux ratio anomalies (see Metcalf et al. 2004 for an example). Even more exciting is the possibility of measuring astrometric shifts along with flux perturbations; further study is needed to determine the feasibility and value of such measurements.

3 PLACING LIMITS ON SUBSTRUCTURE SIZE

While a few lens systems have been observed at many wavelengths, the ones that are most interesting for millilensing are still limited to radio continuum observations (plus perhaps broad-band optical data). Nevertheless, it is still possible to place important *lower* bounds on the substructure responsible for observed flux ratio anomalies. In this section we customize our general analysis of substructure lensing to this application.

3.1 Maximally affected images

We have seen that changing the position of the source relative to the perturber (or vice versa) has a dramatic effect on the magnification versus source size curves. However, in general we do not know the relative position, so it is useful to determine the bounds on the magnification that can be produced by a given perturber for a given source size. In practice, this amounts to setting the ratio b/a of perturber and source sizes (as well as the background field κ and γ), and then maximizing or minimizing the normalized magnification over u_0 and v_0 . Fig. 11a shows the bounds as a function of b/a for a positive parity image with $\kappa = \gamma = 0.3$. For comparison, the solid lines show curves for fixed source positions (from Fig. 7). (The lower bound is trivial, $\mathcal{M} = 1$, since an SIS perturber in front of a positive parity image never produces demagnification.) At small b/a , all of the curves have roughly the same behavior, again illustrating that at large source size the change in magnification is independent of position. At large b/a , \mathcal{M}_{\max} grows to infinity since, in the limit of an infinitesimal source, placing the source on the caustic yields infinite magnification.

The analogous results for a negative parity case are shown in Fig. 11b. Here we have both \mathcal{M}_{\max} and \mathcal{M}_{\min} curves since

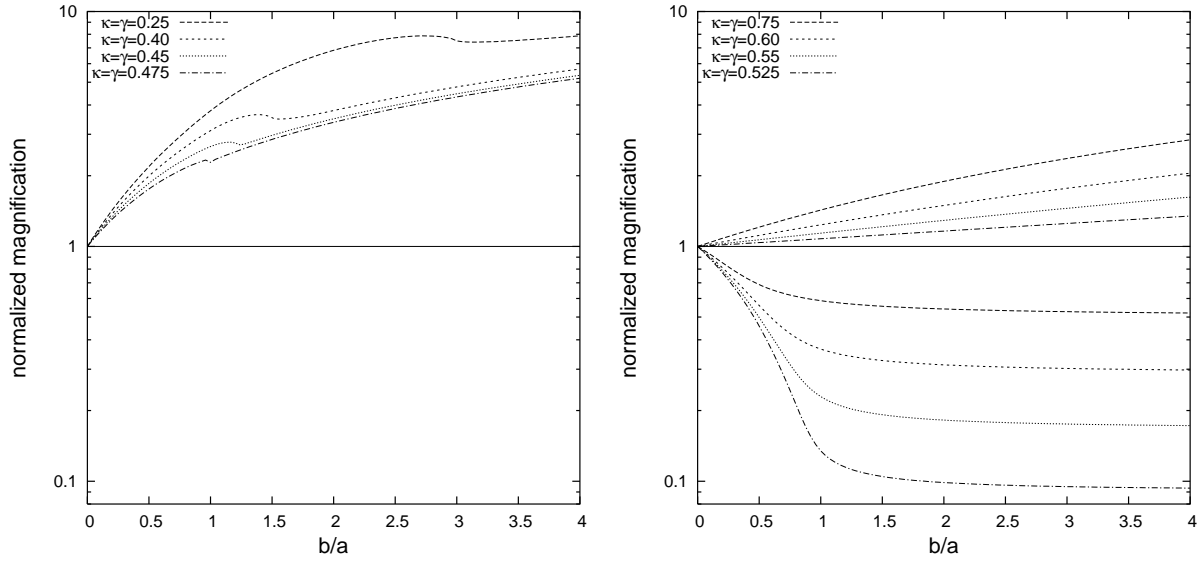


Figure 12. Maximum and minimum normalized magnification versus b/a , for different values of κ and γ .

an SIS in front of a negative parity image can produce both magnification and demagnification.¹ The curves of \mathcal{M} versus b/a at various source position from Fig. 8 are again shown for comparison. An important feature is that the \mathcal{M}_{\min} curve approaches a constant value at large b/a . In the limit of an infinitely small source, a negative parity image allows infinite magnification but *not* infinite demagnification. The shapes of the \mathcal{M}_{\max} and \mathcal{M}_{\min} curves depend on the macromodel through κ and γ , as shown in Fig. 12.

3.2 Limits from a single flux measurement

A key result from Figs 11 and 12 is that we can use any measured $\mathcal{M} \neq 1$ to place a lower bound on b/a , *without needing to know the relative positions of the perturber and source*. This bound comes from the fact that, although the region below the \mathcal{M}_{\max} curve is completely accessible by choosing appropriate values for u_0 and v_0 , the region *above* the \mathcal{M}_{\max} curve is excluded by definition. For any observed $\mathcal{M}_{\text{obs}} > 1$, we simply find the value of b/a where $\mathcal{M}_{\max}(b/a) = \mathcal{M}_{\text{obs}}$, and that gives us the lower limit on the size of the perturber (relative to the size of the source). The bound can be understood physically with the idea that a source cannot ‘feel’ a perturber that is much smaller than itself. Conversely, there is no upper bound because a source that is small relative to the perturber can be placed as far from or as close to the caustics as necessary to reproduce any observed magnification. (Similar reasoning applies to both the magnification and demagnification regimes in the negative parity case.)

For the positive parity case, increasing κ and γ (increasing μ_0) lowers the \mathcal{M}_{\max} curve, or equivalently, increases the minimum value of b/a required to produce a given normalized magnification (see Fig. 12). For the negative parity case, decreasing κ and γ (increasing $|\mu_0|$) lowers both the \mathcal{M}_{\max} and \mathcal{M}_{\min} curves. This is equivalent to increasing the minimum value of b/a required to produce a given $\mathcal{M} > 1$, or decreasing the minimum value of b/a required to produce a given $\mathcal{M} < 1$. Although the lower bound on b/a does depend on κ and γ , these parameters are well constrained by the macromodel (see Fig. 14 below).

If the observed image flux f_{obs} were known precisely, then $\mathcal{M}_{\text{obs}} \equiv f_{\text{obs}}/f_0$ could be used to place a strict lower bound on b/a . Of course, flux measurement uncertainties smear the bound, and the simplest way to incorporate the uncertainties is to define a goodness of fit,

$$\chi_{\text{sub}}^2 \left(\frac{b}{a}; u_0, v_0; \kappa, \gamma \right) = \left[\frac{\mathcal{M}_{\text{mod}}(b/a; u_0, v_0; \kappa, \gamma) - \mathcal{M}_{\text{obs}}}{\sigma_{\text{obs}}} \right]^2. \quad (23)$$

Fig. 13 shows a sample χ^2 analysis, where we generated a mock measurement of $\mathcal{M}_{\text{obs}} = 3.63$ assuming $\kappa = \gamma = 0.3$, $a = b = 5$, $u_0 = v_0 = 0$, and $\sigma_{\text{obs}} = 0.1 \times \mathcal{M}_{\text{obs}}$. In the figure, the solid line shows χ^2 versus b/a if we fix the source at the origin, while the crosses show the result if we optimize over the source position. (We always fix κ and γ , because they are determined well

¹ Again, by magnification or demagnification we mean images brighter or fainter than produced by the convergence and shear field alone.

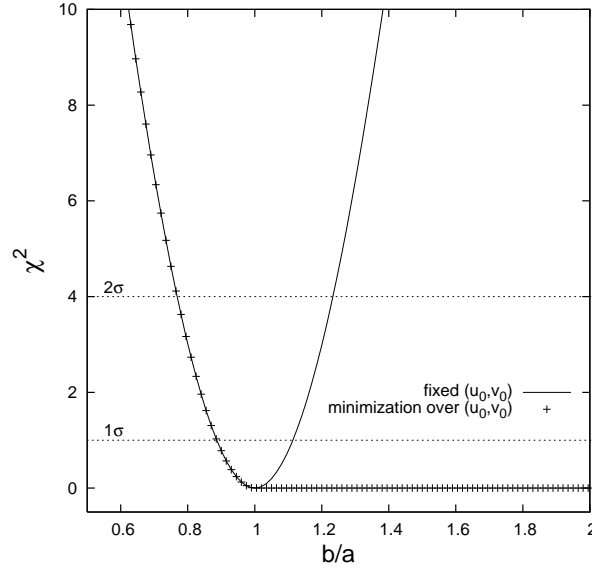


Figure 13. χ^2 versus b/a for a mock measurement of the normalized magnification. The solid line shows the result if we fix the source at its input value, while the crosses show the result if we optimize over the source position.

enough by the macromodel; see §4.2 below.) If the source position were known, we would get both upper and lower limits on b/a . If the source position is unknown, we lose the upper limit but still get the lower limit as discussed above. This is the more interesting limit anyway, since for a given flux ratio anomaly it is useful to know the *smallest possible* perturbing mass that could produce the anomaly.

4 APPLICATION TO OBSERVED LENS SYSTEMS

Before we can apply our millilensing theory to derive substructure mass bounds, we must first figure out which of the images are perturbed. We must also determine the convergence and shear that create the background in which the clump lives. To do this, the idea is to fit a smooth macromodel to an observed lens, identify any images that cannot be fit, and attribute the discrepancy to substructure. We emphasize that this process is independent of any assumptions about the nature of the substructure. It does depend on our choice of macromodel, but the models we use are standard in millilensing analyses (e.g., Dalal & Kochanek 2002; Kochanek & Dalal 2004; Metcalf et al. 2004; Metcalf 2004). Dependence on the substructure model enters only when we bring in the method from §3 to derive constraints on the masses of the substructures.

4.1 Methodology

For the macromodel, we consider two related models. In the first case, we treat the lens galaxy as a singular isothermal ellipsoid (SIE), which is a simple but useful model that is consistent with many lensing, dynamical, and X-ray observations (e.g., Fabbiano 1989; Rix et al. 1997; Gerhard et al. 2001; Treu & Koopmans 2002; Koopmans et al. 2003; Rusin et al. 2003). The model has surface mass density

$$\kappa(r, \theta) = \frac{R_{\text{ein}}}{2r\sqrt{1 - \epsilon \cos 2(\theta - \theta_\epsilon)}}, \quad (24)$$

where R_{ein} is the macromodel Einstein radius, ϵ is an ellipticity parameter related to the axis ratio q of the ellipse by $q^2 = (1 - \epsilon)/(1 + \epsilon)$, and θ_ϵ is the orientation angle of the ellipse major axis. A simple SIE model is insufficient to fit most 4-image lenses, so we add an external shear term to represent the effects of other mass in the environment of the lens galaxy (Keeton, Kochanek, & Seljak 1997). The $N_p = 10$ model parameters are then: the position, Einstein radius, ellipticity, and orientation of the lens galaxy; the amplitude and direction of the external shear; and the position and flux of the source.

In the alternate macromodel, we keep the same monopole but allow a more general angular structure. Expanding the lens potential in multipoles, we write (see Kochanek 2004)

$$\phi(r, \theta) = R_{\text{ein}} r + \frac{R_{\text{ein}}^4}{2r^2} \gamma_{\text{int}} \cos 2(\theta - \theta_{\text{int}}) + \frac{2^2}{2} \gamma_{\text{ext}} \cos 2(\theta - \theta_{\text{ext}}) + \dots \quad (25)$$

The first term is the potential for a singular isothermal sphere (a mass model given by eq. 24 with $\epsilon = 0$). The second term represents the shear due to mass within the Einstein radius, where γ_{int} and θ_{int} are the internal shear amplitude and direction. The third term represents the shear due to mass outside the Einstein radius, which can now include a contribution from the outer parts of the lens galaxy halo in addition to a contribution from the larger lens environment. Compared to the ellipsoid+shear model, the internal+external shear model allows a more general structure for the lens galaxy, but at the expense of not representing true elliptical symmetry very well (since the multipole series is truncated). Both macromodels have the same number of parameters.

We define the macromodel goodness of fit to include contributions from the image positions, the image fluxes, and the galaxy position (if known):

$$\chi_{\text{tot}}^2 = \chi_{\text{pos}}^2 + \chi_{\text{flux}}^2 + \chi_{\text{gal}}^2, \quad (26)$$

$$\chi_{\text{pos}}^2 = \sum_{A,B,C,D} \frac{(\mathbf{x}_{\text{mod}} - \mathbf{x}_{\text{obs}})^2}{\Delta \mathbf{x}_{\text{obs}}^2}, \quad (27)$$

$$\chi_{\text{flux}}^2 = \sum_{A,B,C,D} \frac{(f_{\text{mod}} - f_{\text{obs}})^2}{\Delta f_{\text{obs}}^2}, \quad (28)$$

$$\chi_{\text{gal}}^2 = \frac{(\mathbf{X}_{\text{mod}} - \mathbf{X}_{\text{obs}})^2}{\Delta \mathbf{X}_{\text{obs}}^2}, \quad (29)$$

where \mathbf{x} values are the positions of the images, f values are the fluxes of the images, \mathbf{X} is the position of the galaxy, and Δ indicates measured uncertainties in the respective quantities.

Evidence for substructure is revealed when the macromodel fails to fit the observed fluxes,² but to understand the substructure we need to identify *which* of the images are perturbed. To do that, we systematically relax the flux constraints and refit the macromodel. (We always fit the positions of all four images.) For example, if fitting all four fluxes fails, then we try to fit the fluxes of images A/B/C, then images A/B/D, then A/C/D, and finally B/C/D. If one of those cases, say A/C/D, does provide an acceptable fit, then we settle on the hypothesis that image B is the one most likely to be perturbed by substructure. Should relaxing the flux constraints on one image at a time fail to produce an acceptable fit, we consider the six different possibilities for relaxing two of the flux constraints. (There is no point in relaxing three flux constraints, because the flux of one image can always be fit trivially.) When we fit all four fluxes, the number of constraints on the model is $N_c = 14$ if the galaxy position is known, or $N_c = 12$ if not. With $N_p = 10$ free parameters, we can relax one or two flux constraints and still have a model that is overconstrained or at worst has $\nu = 0$ degrees of freedom.

Once we have found a macromodel that reproduces all of the observed positions and some of the observed fluxes, we interpret the remaining (discrepant) fluxes as evidence for substructure. We characterize the flux perturbation by the ratio $\mathcal{M}_{\text{obs}} = f_{\text{obs}}/f_{\text{mod}}$ of the observed flux to that predicted by the macromodel. We can then plug this value into our substructure analysis to find the smallest size of an SIS clump that could produce that perturbation (as discussed in §3). The substructure analysis depends on the macromodel through the local convergence and shear, but we show below that the statistical uncertainties are small and unimportant for our analysis. In other words, formally we take the substructure goodness of fit from eq. (23), hold κ and γ fixed from the macromodel, and then optimize over u_0 and v_0 to trace out χ_{sub}^2 as a function of b/a . We then use this function obtain a 1σ lower limit on b/a . We conservatively assume 10 per cent flux uncertainties in the substructure analysis, dominated not by measurement uncertainties (which can reach the per cent level; e.g., Fassnacht et al. 2002) but by systematic effects such as time delays. Modifying that assumption would produce a fairly simple change in our mass bounds (see the Appendix), but would not affect our conclusions.

To convert the limit on b/a into a minimum Einstein radius b_{min} and then to a minimum mass within that Einstein radius $M(b)_{\text{min}}$, we must specify a source size a . It has been argued that a lower bound on the size of the emitting region of a quasar in the radio is $a \gtrsim 1$ pc (Wyithe et al. 2002), and that a reasonable size is $a \sim 10$ pc (see Metcalf et al. 2004). The source size does contribute uncertainty to our analysis, but we shall see that it does not really affect our conclusions.

4.2 B1422+231

The 4-image radio and optical lens B1422+231 was the first system identified as likely to contain substructure based on its anomalous flux ratios (Mao & Schneider 1998). The fluxes of images A, B, and C violate the relation $f_A - f_B + f_C \approx 0$ generically expected for a lens in a ‘cusp configuration’ corresponding to a source lying near a cusp caustic (Schneider & Weiss

² Failure to fit the image positions could also provide evidence for substructure (see §2.5), but we expect that in most cases existing data are not good enough to detect this effect. In B1422+231, the position uncertainties from VLBA maps are very precise (Patnaik & Narasimha 2001), but as our formalism is not currently equipped to use astrometric perturbations to constrain substructure, we inflate the errorbars. The ability of astrometry to probe substructure certainly deserves further study.

B1422+231 ellipsoid+shear						
case	Normalized Magnification				χ^2_{tot}	χ^2_{flux}
	Image A	Image B	Image C	Image D		
abcd	1.02	0.993	0.942	0.746	112.97	48.08
abc	1.02	0.998	0.941	0.704	98.34	34.59
abd	1.01	0.986	0.828	0.704	35.08	19.81
acd	1.02	0.961	0.938	0.757	111.19	49.17
bcd	1.21	1.01	0.995	0.925	3.07	0.89
ab	1.00	0.990	0.816	0.649	12.91	0.90
ac	1.02	0.981	0.939	0.704	97.99	35.69
ad	1.00	0.829	0.820	0.793	10.29	6.83
bc	1.21	1.01	0.993	0.909	2.40	0.56
bd	1.19	1.00	0.977	0.909	2.41	1.16
cd	1.23	1.04	1.00	0.909	1.71	0.94

Table 1. Modeling results for B1422+231 using an ellipsoid+shear macromodel. Column 1 lists the image fluxes that were used to constrain the macromodel. Columns 2–5 list \mathcal{M}_{obs} , or the ratio of the observed magnification to that predicted by the macromodel, for the four images. Columns 6–7 give the total χ^2 and the contribution from the fluxes.

1992; Mao 1992; but see Keeton et al. 2003). To model the lens, we use the image positions and fluxes from the 8.4 GHz observations by Patnaik et al. (1999). Their VLBA maps yield very precise relative positions, but we conservatively inflate the uncertainties to 5 mas because we do not study astrometric perturbations in detail in this paper (see §2.5). The radio fluxes are essentially constant (see Patnaik & Narasimha 2001), so we can neglect systematics and use the flux measurement uncertainties quoted by Patnaik et al. (1999). We use radio rather than optical fluxes because they should be sensitive only to dark matter substructure (not to microlensing by stars). For the lens galaxy, we use the position given by CASTLES.³

Table 1 shows our results for fitting the system with an ellipsoid+shear macromodel. Fitting the fluxes of all four images gives a very poor fit ($\chi^2/\nu = 113/4$), so we relax the flux constraints one at a time to consider the possibility that one of the images might be perturbed by substructure. Fitting the fluxes of A, C, and D yields an equally bad fit, so we can rule out the hypothesis that only image B is perturbed by substructure. The same result holds if we fit ABC or ACD. However, if we consider A to be perturbed, then we get a good fit with $\chi^2/\nu = 3.1/3$.

We then apply our substructure analysis to this model to find the minimum clump mass required to perturb image A. The macromodel has convergence $\kappa = 0.381$ and shear $\gamma = 0.496$ at the position of image A. In order to produce a perturbation of $\mathcal{M}_{\text{obs}} = 1.213$, an SIS clump in this convergence and shear field must have $b/a > 0.0561$ (1σ). Given the source redshift $z_s = 3.62$ and lens redshift $z_l = 0.34$, this b/a bound translates to a mass within the Einstein radius of $M(b) > 2.07 \times 10^3 (a/10 \text{ pc})^2 M_\odot$, or equivalently to a velocity dispersion of $\sigma > 2.24 (a/10 \text{ pc}) \text{ km s}^{-1}$. We emphasize that we are quoting the mass within the Einstein radius, and the total clump mass may be much larger. The large lower limit on the perturber mass confirms and quantifies the conventional wisdom that microlensing cannot explain radio flux ratio anomalies.

The substructure analysis does depend on the macromodel, through the local convergence and shear at the position of image A. There is an uncertainty in the macromodel between the ellipticity and external shear which leads to an uncertainty in κ and γ , as shown in Fig. 14. The effect is small, however: over the 1σ confidence region of the macromodel, κ varies by about 0.01 and γ varies by about 0.025. This small variation affects the mass bound by only ~ 8 per cent, and the velocity dispersion bound by even less. Another uncertainty in the macromodel arises from the mass sheet degeneracy, but we saw in §2.4 that this has no effect on our substructure analysis. In other words, the macromodel is constrained well enough for our purposes.

If we allow for the possibility of clumps in front of more than one image, we find that there are three models that give a good fit to the data (BC, BD, and CD; see Table 1). All three models still require substructure in front of image A, with mass bounds similar to that found for the BCD model. For each model, the 1σ lower limit on the mass in front of the other image is zero. That is, we can generically conclude that there must be a clump of mass $M(b) > 2 \times 10^3 M_\odot$ in front of image A, and there is no evidence of clumps in front of any other images.

³ CfA/Arizona Space Telescope Lens Survey; see <http://cfa-www.harvard.edu/castles>.

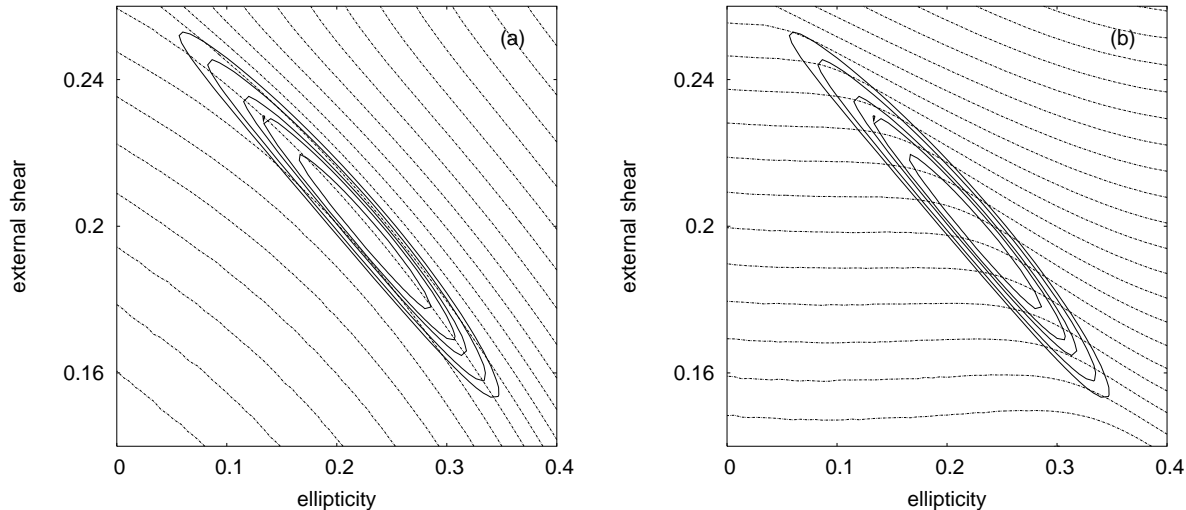


Figure 14. The ellipses show χ^2 contours for B1422+231 in the ellipticity-shear plane, showing the 1σ , 90 per cent, 2σ , 99 per cent, and 3σ confidence regions. The dotted contours are (a) κ and (b) γ contours plotted in intervals of $\delta\kappa = \delta\gamma = 0.005$. The small variation in κ and γ over the ellipses implies that uncertainties in the substructure analysis due to the macromodel are small.

B2045+265 ellipsoid+shear						
case	Normalized Magnification				χ^2_{tot}	χ^2_{flux}
	Image A	Image B	Image C	Image D		
abcd	1.80	0.726	3.14	17.32	172.17	171.24
abc	1.84	0.744	3.22	17.59	81.80	80.48
abd	1.99	0.805	3.48	18.75	124.29	122.21
acd	0.796	0.321	1.39	7.46	93.05	90.94
bcd	2.05	0.828	3.58	19.33	150.05	148.05
ab	2.06	0.829	3.59	20.00	31.55	30.77
ac	0.844	0.339	1.47	8.21	14.43	13.66
ad	0.912	0.367	1.59	8.54	82.57	80.45
bc	2.12	0.856	3.71	20.67	56.97	56.19
bd	2.38	0.960	4.15	22.41	95.25	93.28
cd	0.497	0.200	0.869	4.63	67.29	65.02

Table 2. Modeling results for B2045+265 using an ellipsoid+shear macromodel.

4.3 B2045+265

B2045+265 is a 4-image radio and optical lens with the source quasar at redshift $z_s = 1.28$ and the lens galaxy at redshift $z_l = 0.87$ (Fassnacht et al. 1999). It is the tightest known cusp configuration lens, and it exhibits a strong violation of the cusp relation in both radio and optical bands (Keeton et al. 2003). We seek to fit the 5 GHz MERLIN radio data from Fassnacht et al. (1999), taking radio component E to indicate the position of the lens galaxy.

Table 2 shows the results of modeling this system with an ellipsoid+shear macromodel. Attempting to fit all of the positions and fluxes gives a very bad fit ($\chi^2/\nu = 172/4$). Relaxing some of the flux constraints yields somewhat better fits, with the best case being when we only fit the fluxes of images A and C ($\chi^2/\nu = 14.4/2$). However, all of these models underpredict the flux of image D, by as much as a factor of 20, implying that there must be a clump producing a very large perturbing magnification. The problem is that when a clump is placed in front of a negative parity image like D, the cross section for significant magnification is very small. Therefore, the large magnifications shown in these models would require a very massive clump in a very particular position. Not only would such a large perturbing mass almost certainly result in resolvable splittings of image D that are not observed, it would probably affect the positions and fluxes of the other images as well.

These problems lead us to consider the alternate internal+external shear macromodel, whose results are given in Table 3. Trying to fit all of the fluxes still gives a poor fit ($\chi^2/\nu = 90/4$). Dropping one of the flux constraints improves the fit, but

B2045+265 internal+external shear						
case	Normalized Magnification				χ^2_{tot}	χ^2_{flux}
	Image A	Image B	Image C	Image D		
abcd	1.88	0.743	3.31	1.00	89.57	82.72
abc	1.72	0.741	2.81	354.38	71.89	71.40
abd	2.09	0.827	3.68	1.00	38.66	31.74
acd	0.841	0.333	1.48	1.00	20.25	14.09
bcd	2.17	0.856	3.81	1.00	64.26	57.31
ab	1.93	0.829	3.15	381.13	28.03	27.53
ac	0.852	0.365	1.39	166.94	11.42	10.92
ad	0.995	0.393	1.75	1.00	6.31	0.00
bc	1.97	0.846	3.21	396.07	51.22	50.72
bd	2.52	0.996	4.44	1.00	7.05	0.00
cd	0.565	0.224	0.994	1.00	5.74	0.01

Table 3. Modeling results for B2045+265 using an internal+external shear macromodel.

even the best case is still not an acceptable fit (the ACD model has $\chi^2/\nu = 20/3$). Dropping two flux constraints, however, yields three acceptable models. Fitting A and D gives $\chi^2/\nu = 6.31/2$, fitting B and D gives $\chi^2/\nu = 7.05/2$, and fitting C and D gives $\chi^2/\nu = 5.74/2$; all three models differ from the data by only $\sim 2\sigma$. Although the CD case has the lowest χ^2 , it requires the positive parity A image to be demagnified by about a factor of two, which is not possible with an SIS clump. So we are only left with the AD and BD cases as viable models for the system. The AD model has substructure perturbing masses in front of images B ($\mathcal{M}_{\text{obs}} = 0.3938$) and C ($\mathcal{M}_{\text{obs}} = 1.7518$) while the BD model has perturbers in front of images A ($\mathcal{M}_{\text{obs}} = 2.5283$) and C ($\mathcal{M}_{\text{obs}} = 4.4474$).

The results of applying our substructure analysis are shown in Table 4. In the BD model, the substantial magnifications of images A and C require large clumps: the mass in front of A must be larger than $2.29 \times 10^6 M_{\odot}$ ($\sigma > 15.51 \text{ km s}^{-1}$), and the mass in front of image C must be larger than $1.58 \times 10^7 M_{\odot}$ ($\sigma > 25.12 \text{ km s}^{-1}$). In the AD model, the minimum masses necessary to reproduce the anomalous fluxes are somewhat smaller: $M(b) > 4.77 \times 10^5 M_{\odot}$ ($\sigma > 10.78 \text{ km s}^{-1}$) for image B, and $M(b) > 3.71 \times 10^5 M_{\odot}$ ($\sigma > 9.84 \text{ km s}^{-1}$) for image C. (We have again assumed a source size $a = 10 \text{ pc}$.) Although we cannot identify a unique model, the important points are that the clump masses are $\gg M_{\odot}$ and therefore exclude microlensing as an explanation for the observed flux ratio anomalies, and also that they agree well with the sizes of clumps predicted by a Λ CDM cosmology (e.g., Klypin et al. 1999; Moore et al. 1999).

The mass bounds given above were calculated for a clump lying within halo of the main lens galaxy. It is possible, though, that the clump lies elsewhere along the line of sight (Keeton 2003; Metcalf 2004); the likelihood depends on the relative abundances of embedded and isolated clumps (see Chen et al. 2003). As discussed in §2, our formalism can easily accommodate the hypothesis that the clump lies at redshift $z_c \neq z_l$ (see eq. 3). Fig. 15 shows how the clump bounds for images B and C vary with clump redshift for the AD internal+external shear model. Moving the clump in redshift away from the lens galaxy increases the lower bound on b/a for negative parity image B, and decreases it for positive parity image C. (These dependences can be understood in terms of eq. 3 and Fig. 12.) However, the effect is only tens of percent over a wide range in redshift. A stronger variation is seen in the mass bound, because of the additional redshift dependence in the lensing critical density ($\Sigma_{\text{cr}} \propto D_{\text{os}}/D_{\text{ol}}D_{\text{os}}$). Even so, the change is a factor of a few, so uncertainty in the location of the clump along the line of sight does not significantly affect order of magnitude conclusions.

4.4 B1555+375

B1555+375 is a faint 4-image radio lens discovered by Marlow et al. (1999), whose fluxes violate the relation $f_A - f_B \approx 0$ expected for a lens in a ‘fold configuration’ (Gaudi et al. 2005). We fit the 5 GHz data from Marlow et al. The position of the lens galaxy with respect to the images has not been measured. The lens and source redshifts are not known, but Marlow et al. estimate them to lie in the ranges $1.0 \lesssim z_s \lesssim 3.0$ and $0.5 \lesssim z_l \lesssim 1.0$.

Our attempts to fit this system with an ellipsoid+shear macromodel result in models with very large and perpendicularly aligned ellipticities and shears ($e \sim 0.9$, $\gamma_{\text{ext}} \sim 0.3$, and $\Delta\theta = 90^\circ$). These models are highly contrived, and have extremely large and implausible magnifications. We consider them to be unphysical, and turn instead to internal+external shear macromodels.

Fitting all four images yields a model with $\chi^2/\nu = 45.6/2$ that reproduces the image positions well but not the flux ratios. Relaxing the flux constraints in front of one image can improve the fit, but the resulting models are unacceptable in that they require the positive parity image A to be demagnified or the negative parity image D to be highly amplified by a

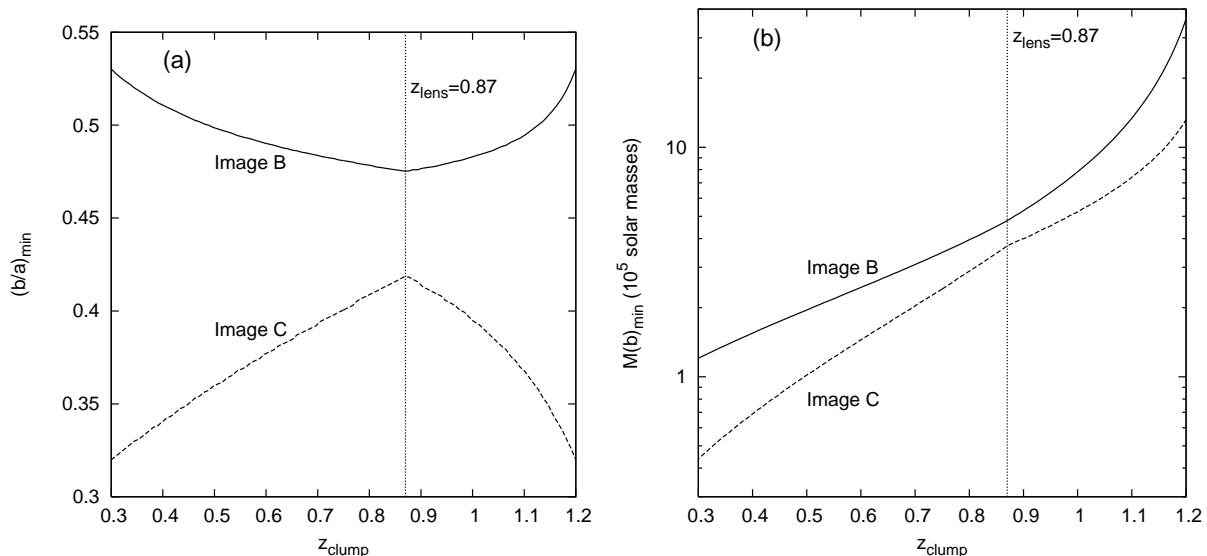


Figure 15. Dependence of the clump bound on the clump redshift, for the two perturbed images in the AD internal+external shear model for B2045+265. (a) The lower bound on b/a . (b) The lower bound on the mass within the Einstein radius, $M(b)$.

Lens	Macromodel	Perturbed Image(s)	χ^2/ν	Image	$M(b)_{\min}$ (M_{\odot})	σ_{\min} (km s^{-1})
B1422+231	ellipsoid+shear	A	3.073/3	A	2.07×10^3	2.24
B2045+265	internal+external shear	A and C	7.051/2	A	2.29×10^6	15.51
				C	1.58×10^7	25.12
		B and C	6.320/2	B	4.77×10^5	10.48
		C		3.71×10^5	9.84	
B1555+375	internal+external shear	A and C	1.045/0	A	1.96×10^5	7.14
				C	3.54×10^6	14.72
		B and C	0.000/0	B	1.19×10^5	6.30
		C		5.08×10^4	5.09	

Table 4. The 1σ lower limits on the mass within the Einstein radius and the velocity dispersion of perturbing clumps. There is only one acceptable model for B1422+231, but there are two possibilities for B2045+265 and B1555+375. The bounds scale with the assumed source size as $M(b)_{\min} \propto (a/10 \text{ pc})^2$ and $\sigma_{\min} \propto (a/10 \text{ pc})$.

clump. The only acceptable models are found when we relax two flux constraints, and in fact there are two good cases (see Table 4). One possibility is to have a clump in front of image B with $b/a > 0.328$, plus a clump in front of image C with $b/a > 0.214$. This model fits the data perfectly, which is not surprising because it has $\nu = 0$ degrees of freedom. Assuming redshifts of $z_s = 2.0$ and $z_l = 0.75$, the b/a bounds translate into clump mass limits of $M > 1.19 \times 10^5 M_{\odot}$ ($\sigma > 6.30 \text{ km s}^{-1}$) and $M > 5.08 \times 10^4 M_{\odot}$ ($\sigma > 5.09 \text{ km s}^{-1}$) for images B and C, respectively. Varying the redshifts can change the mass limits by a factor of a few up to ~ 10 , but does not affect the conclusion that the fluxes cannot be explained by microlensing. The other possibility is to have a clump in front of image A with $b/a > 0.420$ ($M > 1.96 \times 10^5 M_{\odot}$, or $\sigma > 7.14 \text{ km s}^{-1}$), plus a clump in front of image C with $b/a > 1.783$ ($M > 3.54 \times 10^6 M_{\odot}$, or $\sigma > 14.72 \text{ km s}^{-1}$). This model gives $\chi^2 = 1.045$ for $\nu = 0$, which is formally unacceptable. However, as an exercise we added random noise to the data and refit. A substantial fraction of these cases yielded $\chi^2 = 0$, which suggests that the model is in fact consistent with the data given the measurement uncertainties.

4.5 B0712+472

B0712+472 is a 4-image lens with an image configuration intermediate between a cusp and fold (Jackson et al. 1998). The optical flux ratios strongly violate the cusp and fold relations, but at radio wavelengths the violation is marginal (Keeton et al.

B0712+472						
case	internal+external shear			ellipsoid+shear		
	χ^2_{tot}	χ^2_{flux}	F-test	χ^2_{tot}	χ^2_{flux}	F-test
abcd	7.29	1.49	$\equiv 1.00$	18.83	9.37	$\equiv 1.00$
abc	7.06	1.41	0.85	14.59	7.94	0.20
abd	4.51	0.98	0.08	10.34	7.00	0.06
acd	6.59	2.96	0.50	9.42	2.26	0.04
bcd	6.48	0.63	0.44	6.06	0.03	0.02
ab	2.88	1.20	0.06	2.22	1.63	0.01
ac	6.48	2.95	0.49	3.46	0.01	0.02
ad	2.42	0.73	0.05	2.02	0.02	0.01
bc	6.44	0.65	0.47	4.10	0.00	0.03
bd	4.48	0.99	0.14	2.88	0.02	0.02
cd	0.72	0.11	0.01	0.98	0.02	0.01

Table 5. Modeling results for B0712+472 using both macromodels. The F-test gives the probability that χ^2 has decreased (relative to the abcd model) only because the model has fewer constraints, rather than because the fit is significantly better.

2003; Gaudi et al. 2005). The difference suggests that the optical flux ratios are affected by microlensing. We focus on the radio flux ratios, and fit the data given by Jackson et al. (2000). As shown in Table 5, attempting to fit all four radio fluxes yields $\chi^2/\nu = 18.77/4$ for an ellipsoid+shear macromodel, or $\chi^2/\nu = 7.29/4$ for an internal+external shear macromodel. The internal+external shear model differs from the data at only 88 per cent confidence, so it is a reasonably good fit. Nevertheless, it is interesting to consider whether the fit can be improved by relaxing the flux constraints, as shown in Table 5. Among three-flux models, only ABD yields a noticeably better fit. Among two-flux models, only the AD case yields a reasonable model that gives a better fit. (The AB model can be ruled out because it requires the negative parity image D to be magnified by a factor of ~ 20 relative to the macromodel; while the CD model can be ruled out because it requires the positive parity image A to be demagnified by a factor of ~ 2 .)

Although we see that relaxing flux constraints lowers the χ^2 , we must ask whether that really provides evidence for substructure, or whether it just indicates that we are using fewer constraints. The test for statistical significance when removing degrees of freedom is called the F-test (e.g., Bevington & Robinson 1992). The F-test returns a probability that the change in χ^2 is due simply to the change in the number of degrees of freedom – so a *low* value of the probability indicates that the fit really has improved. The test results are given in Table 5, and they confirm our intuition that many of the three-flux and two-flux models are not significantly better than the ABCD model. However, the ABD and AD models have relatively low F-test values (0.08 and 0.05, respectively), so we conclude that there is marginal evidence for a radio flux ratio anomaly, and if real it is probably in image C.

5 CONCLUSIONS

We have developed a semi-analytic formalism for computing the effects of substructure on the lensed images of a finite-size source. By considering the local effects of a clump modeled as an isothermal sphere, we can solve analytically for the perturbed micro-image(s), and then compute numerically the change in the position and magnification of the macro-image. While this is a simplified toy model, it yields valuable insight into the general features of finite source effects in substructure lensing:

- The perturbations do not have a simple dependence on source size, but are related to intersections of the source with micro-caustics.
- Positive parity images are always amplified by isothermal clumps, but negative parity images may be either amplified or suppressed depending on the source position and size.
- Sources that are more than an order of magnitude larger than the clump Einstein radius can still be perturbed at the percent level, which mildly contradicts conventional wisdom that a source cannot ‘feel’ lensing structure on scales smaller than itself.
- Statistical uncertainties in the macromodel do not significantly affect the substructure analysis. Remarkably, the mass sheet degeneracy in the macromodel has *no effect* on the substructure analysis, at least for isothermal clumps.
- Astrometric perturbations could be at the few milli-arcsec level, and could be identified by comparing the relative image positions at different wavelengths.

The bottom line is that there is a tremendous amount to be learned from high-resolution observations at a variety of wavelengths that correspond to different source sizes. The promising possibilities are observations of the optical, mid-IR, and radio continua, and the optical emission lines. (Detailed X-ray observations seem less valuable, because the source will be much smaller than the caustics for millilensing.) The first steps in this direction have been taken (Agol et al. 2000; Wisotzki et al. 2003; Metcalf et al. 2004), but a more concerted effort to do this for flux ratio anomaly lenses is called for.

It is already possible to place limits on the substructure mass scale: since there is a finite range of magnifications possible for a given ratio of the clump Einstein radius b to the source size a , an observed flux perturbation leads directly to a lower bound on b/a (even with no knowledge of the relative positions of perturber and source). Adding knowledge of (or assumptions about) the source size then leads to a lower bound on the clump mass. These substructure bounds do depend on our assumption that each flux ratio anomaly is caused by a single, isolated, isothermal clump; how they change for different clump models and for the limit of moderate or high optical depth will be the subject of a follow-up study. Still, the principle that finite source effects permit simple *lower* bounds on the substructure mass scale should be general.

With this background, we have sought to understand three known lensing systems with strong flux ratio anomalies at radio wavelengths (B1422+231, B1555+375, and B2045+265), plus one system with marginal evidence for a radio flux ratio anomaly (B0712+472). We carefully examined macromodels consisting of an isothermal lens galaxy with different types of angular structure, in order to determine which of the lensed images are perturbed and by how much. Assuming isothermal clumps, we could then use our substructure analysis to place lower bounds on the clump masses. For B1422+231, we find strong evidence for a clump in front of image A, and the mass within the clump Einstein radius must be $M > 2 \times 10^3 (a/10 \text{ pc})^2 M_\odot$. For B2045+265 and B1555+375, we find strong evidence for clumps in front of *two* images in each system. The masses within the Einstein radii are $M \gtrsim 10^4\text{--}10^7 M_\odot$, which generally agrees with Λ CDM predictions, although it is important to consider whether Λ CDM predicts enough clumps to explain the presence of multiple anomalies in multiple lenses. In B0712+472, there is marginal evidence for a clump in front of image C. We emphasize that our identification of the images that are perturbed is independent of assumptions about the nature of substructure; those assumptions enter only when we derive quantitative clump mass bounds.

To round out our analysis, we have considered several systematic effects in the substructure mass bounds. As noted above, statistical uncertainties in the macromodel propagate into the substructure analysis, but their effects are small. In many lensing applications the main problem is the mass sheet degeneracy in the macromodel, but we have shown that it has no effect on the substructure analysis, at least for isothermal clumps. Thus, it turns out that the main systematics are the uncertainty in the source size, and lack of knowledge about whether the clump lies within the main lens galaxy (a standard assumption) or elsewhere along the line of sight. Varying the clump redshift over a reasonable range can change the clump mass bounds by a factor of a few. So it is certainly important for detailed quantitative results, but not so important for order of magnitude reasoning.

Ultimately, using flux ratio anomalies to test Λ CDM and draw conclusions about the nature of dark matter relies on sophisticated statistical analyses with realistic clump models (e.g., Dalal & Kochanek 2002; Kochanek & Dalal 2004; Metcalf et al. 2004). Toy models like ours are still valuable, though, because they reveal and clarify the general principles on which the sophisticated analyses are based. For example, our results suggest that looking for effects requiring comparable scales for the source size and the lensing substructure will be the best way to distinguish the substructure explanation for flux ratio anomalies from competing hypotheses that may be disfavored but not yet ruled out. Furthermore, we believe that a detailed understanding of flux ratio anomalies in individual lenses will always be an important complement to ‘black box’ statistical machinery.

REFERENCES

- Abajas C., Mediavilla E., Muñoz J. A., Popovic L. C., Oscoz A., 2002, ApJ, 576, 640
 Agol E., Jones B., Blaes O., 2000, ApJ, 545, 657
 Benson A. J., Frenk C. S., Lacey C. G., Baugh C. M., Cole S., 2002, MNRAS, 333, 177
 Bevington P. R., Robinson D. K., 1992, Data reduction and error analysis for the physical sciences. McGraw-Hill, New York
 Bullock J. S., Kravtsov A. V., Weinberg D. H., 2000, ApJ, 539, 517
 Chang K., Refsdal S., 1979, Nat, 282, 561
 Chen J., Kravtsov A. V., Keeton C. R., 2003, ApJ, 592, 24
 Colín P., Avila-Reese V., Valenzuela O., 2000, ApJ, 542, 622
 Cooray A., Sheth R. K., 2002, Phys Rep, 372, 1
 Dalal N., Kochanek C. S., 2002, ApJ, 572, 25
 Dodelson S. et al., 2002, ApJ, 572, 140
 Evans N. W., Witt H. J., 2003, MNRAS, 345, 1351
 Fabbiano G., 1989, ARA&A, 27, 87

- Fassnacht C. D. et al., 1999, *AJ*, 117, 658
- Fassnacht C. D., Xanthopoulos E., Koopmans L. V. E., Rusin D., 2002, *ApJ*, 581, 823
- Finch T. K., Carlivati L. P., Winn J. N., Schechter P. L., 2002, *ApJ*, 577, 51
- Gaudi B. S., Keeton C. R., Petters A. O., 2005, in preparation
- Gerhard O., Kronawitter A., Saglia R. P., Bender R., 2001, *AJ*, 121, 1936
- Gorenstein M. V., Shapiro I. I., Falco E. E., 1988, *ApJ*, 327, 693
- Inoue K. T., Chiba M., 2004, preprint (astro-ph/0411168)
- Jackson N. et al., 1998, *MNRAS*, 296, 483
- Jackson N., Xanthopoulos E., Browne I. W. A., 2000, *MNRAS*, 311, 389
- Keeton C. R., 2003, *ApJ*, 584, 664
- Keeton C. R., Zabludoff A. I., 2004, *ApJ*, 612, 660
- Keeton C. R., Kochanek C. S., Seljak U., 1997, *ApJ*, 482, 604
- Keeton C. R., Gaudi B. S., Petters A. O., 2003, *ApJ*, 98, 138
- Klypin A., Kravtsov A. V., Valenzuela O., Prada F., 1999, *ApJ*, 522, 82
- Kochanek C. S., 1991, *ApJ*, 373, 354
- Kochanek C. S., 2004, in Meylan G., Jetzer P., North P., eds., *Proc. 33rd Saas-Fee Advanced Course, Gravitational Lensing: Strong, Weak & Micro*. Springer-Verlag, Berlin; also preprint (astro-ph/0407232)
- Kochanek C. S., Dalal N., 2004, *ApJ*, 610, 69
- Koopmans L. V. E., Treu T., Fassnacht C. D., Blandford R. D., Surpi G., 2003, *ApJ*, 599, 70
- Krolik J. H., 1999, *Active Galactic Nuclei: From the Central Black Hole to the Galactic Environment*. Princeton University Press, Princeton, NJ
- Lewis G. F., Ibata R. A., 2004, *MNRAS*, 348, 24
- Mao S., 1992, *ApJ*, 389, 63
- Mao S., Schneider P., 1998, *MNRAS*, 295, 587
- Mao S., Jing Y. P., Ostriker J. P., Weller J., 2004, *ApJ*, 604, L5
- Marlow D. R. et al., 1999, *AJ*, 118, 654
- Metcalf R. B., Madau P., 2001, *ApJ*, 563, 9
- Metcalf R. B., 2002, *ApJ*, 580, 696
- Metcalf R. B., Moustakas L. A., Bunker A. J., Parry I. R., 2004, *ApJ*, 607, 43
- Metcalf R. B., 2004, preprint (astro-ph/0407298)
- Moore B., Ghigna S., Governato F., Lake G., Quinn T., Stadel J., Tozzi P., 1999 *ApJ*, 524, L19
- Moustakas L. A., Metcalf R. B., 2003, *MNRAS*, 339, 607
- Navarro J. S., Frenk C. S., White S. D. M., 1996, *ApJ*, 462, 563
- Patnaik A. R., Narasimha D., 2001, *MNRAS*, 326, 1403
- Patnaik A. R., Kembal A. J., Porcas R. W., Garrett M. A., 1999, *MNRAS*, 307, L1
- Peterson B. M., 1997, *An Introduction to Active Galactic Nuclei*. Cambridge University Press, New York
- Refsdal S., 1964, *MNRAS*, 128, 307
- Richards G. T. et al., 2004, *ApJ*, 619m 679
- Rix H.-W., de Zeeuw P. T., Carollo C. M., Cretton N., van der Marel R. P., 1997, *ApJ*, 488, 702
- Rusin D., Kochanek C. S., Keeton C. R., 2003, *ApJ*, 595, 29
- Saha P., 2000, *AJ*, 120, 1654
- Schechter P. L., Wambsganss J., 2002, *ApJ*, 580, 685
- Schneider P., Weiss A., 1992, *A&A*, 260, 1
- Sheth R. K., Jain B., 2003, *MNRAS*, 345, 529
- Somerville R. S., 2002, *ApJ*, 572, L23
- Spergel D. N., Steinhardt P. J., 2000, *PRL*, 84, 3760
- Spergel D. N. et al., 2003, *ApJS*, 148, 175
- Tegmark M. et al., 2002, *ApJ*, 571, 191
- Treu T., Koopmans L. V. E., 2002, *ApJ*, 575, 87
- Treyer M., Wambsganss J., 2004, *A&A*, 416, 19
- Wambsganss J., 2001, *PASA*, 18, 207
- Winn J. N., Rusin D., Kochanek C. S., 2004, *Nat*, 427, 613
- Wisotzki L. et al., 2003, *A&A*, 408, 455
- Wyithe J. S. B., Agol E., Fluke C. J., 2002, *MNRAS*, 331, 1041
- Young P., Gunn J. E., Kristian J., Oke J. B., Westphal J. A., 1981, *ApJ*, 244, 736

APPENDIX A: BEHAVIOR AT LARGE SOURCE SIZE

A1 Taylor series expansion of the magnification

We noted in §2.4 that at large a the magnification appeared to be roughly independent of source position. We now confirm rigorously that it is independent of source position to first order in $1/a$. First, we define some quantities to simplify the notation:

$$\begin{aligned} c_1 &= 2u_0(1 - \kappa - \gamma) \cos \theta + 2b(1 - \kappa - \gamma \cos 2\theta) + 2v_0(1 - \kappa + \gamma) \sin \theta \\ c_2 &= b^2 + u_0^2 + v_0^2 + 2b u_0 \cos \theta + 2b v_0 \sin \theta \\ c_3 &= 4[u_0(1 - \kappa - \gamma) \cos \theta + b(1 - \kappa - \gamma \cos 2\theta) + v_0(1 - \kappa + \gamma) \sin \theta]^2 \\ d_1 &= 4[(1 - \kappa)^2 + \gamma^2 - 2\gamma(1 - \kappa) \cos 2\theta] \end{aligned}$$

Note that c_1 , c_2 , and c_3 all depend on the source position, while d_1 does not. With these definitions, we can write

$$\frac{r_{\pm}(\theta)}{a} = \frac{2}{d_1} \left(\xi c_1 \pm \sqrt{(c_3 - c_2 d_1) \xi^2 + d_1} \right), \quad (\text{A1})$$

where $\xi \equiv 1/a$. We immediately see that as $a \rightarrow \infty$ ($\xi \rightarrow 0$), r_-/a is negative while r_+/a is positive and finite, so the image boundary is formed only by r_+ , and the magnification $\mathcal{M} \propto \int [r_+(\theta)/a]^2 d\theta$ remains finite. Expanding in ξ , we find:

$$\begin{aligned} \mathcal{M} &= \frac{(1 - \kappa)^2 - \gamma^2}{2\pi} \int \left(\frac{r_+(\theta)}{a} \right)^2 d\theta \\ &= \frac{(1 - \kappa)^2 - \gamma^2}{2\pi} \int \left[\frac{4}{d_1} + \frac{8c_1}{d_1^{3/2}} \xi + \mathcal{O}(\xi^2) \right] d\theta \\ &= 1 + \xi \frac{(1 - \kappa)^2 - \gamma^2}{2\pi} \int \frac{2b(1 - \kappa - \gamma \cos 2\theta)}{[(1 - \kappa)^2 + \gamma^2 - 2\gamma(1 - \kappa) \cos 2\theta]^{3/2}} d\theta + \mathcal{O}(\xi^2) \end{aligned} \quad (\text{A2})$$

where in the last step we used the fact that any periodic function whose period is an odd multiple of π integrates to zero. The zeroth order term shows that a sufficiently large source is insensitive to the perturber; it has a normalized magnification $\mathcal{M} \approx 1$, meaning that it only feels the convergence and shear field. In the first order term, the integral cannot be evaluated analytically, but the important result is that it does not depend on the source position (u_0, v_0). Thus, to first order in $1/a$, the magnification is independent of source position. Carrying the expansion further reveals that u_0 and v_0 enter only at second order in $1/a$.

A2 Substructure limits at large source size

The series expansion of the normalized magnification can be combined with eq. (23) to obtain an analytic result for the minimum size of the perturbing mass from a single flux measurement. The expansion has the form $\mathcal{M}_{\text{obs}} \approx 1 + C(b/a)$ where C is a number that depends on κ and γ . Using this in the definition of the substructure χ^2 , we find that the upper and lower bounds on b can be written as

$$b_{\pm} \approx \frac{a}{C} \left(\mathcal{M}_{\text{obs}} - 1 \pm \sigma_{\text{obs}} \sqrt{\chi^2} \right), \quad (\text{A3})$$

where $\sqrt{\chi^2}$ indicates the confidence level desired (e.g., $\sqrt{\chi^2} = N$ for N - σ). Fig. A1 compares this analysis to the exact χ^2 analysis used in the main paper, and shows that it recovers reasonably accurate lower limits on b even for sources as small as $a/b \sim 5$.

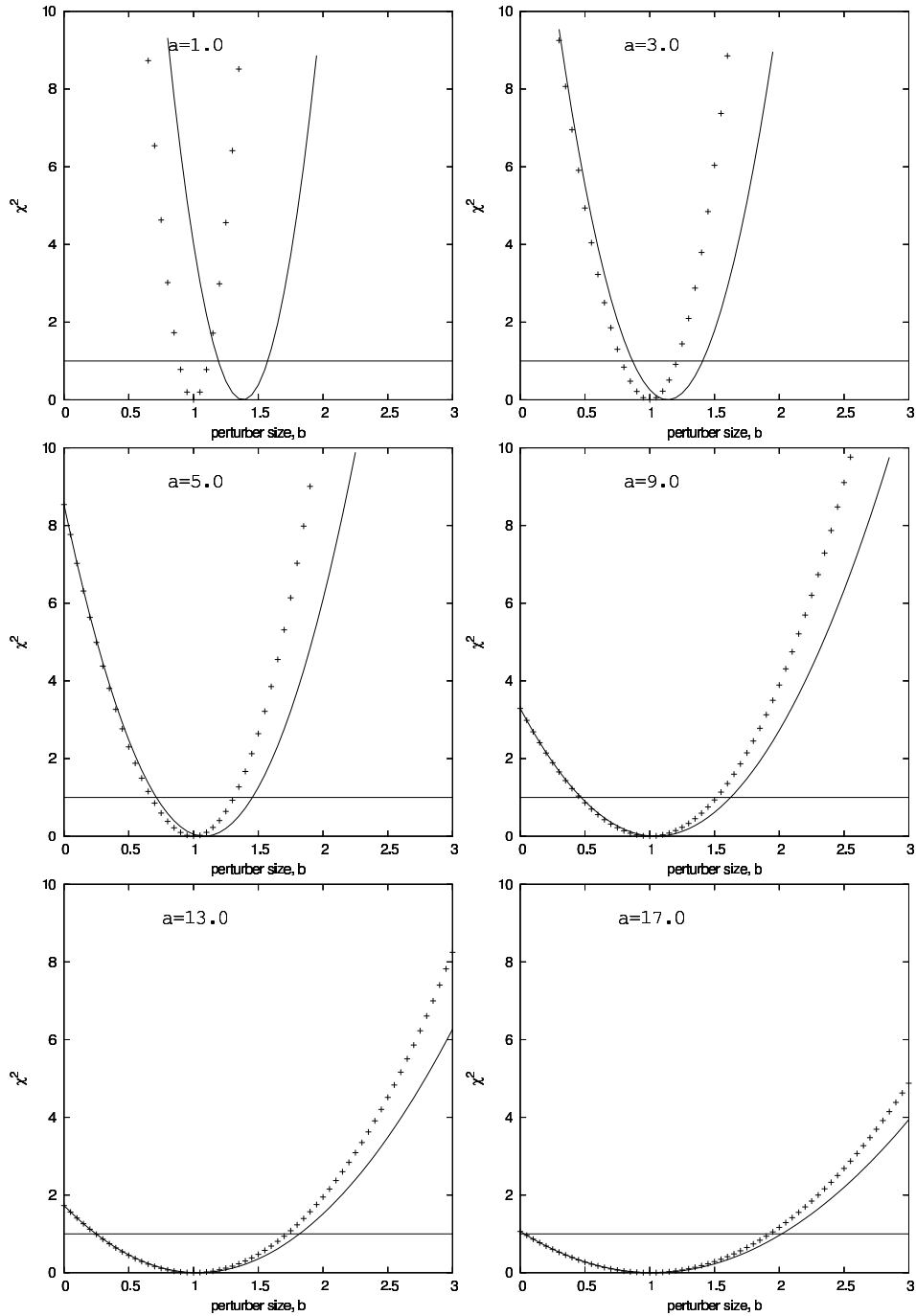


Figure A1. χ^2 as a function of perturber size for various a . The crosses represent the exact analysis (holding the source position fixed), while the solid lines represent the analysis using the first order Taylor series expansion of the model magnification. The expansion analysis gives approximately the correct 1σ lower limit on b for $a \gtrsim 5$.